

Figures

All figures can be found in color on the accompanying DVD in the 'Figures' folder and in the 'Figures.doc' text file, which includes the captions.

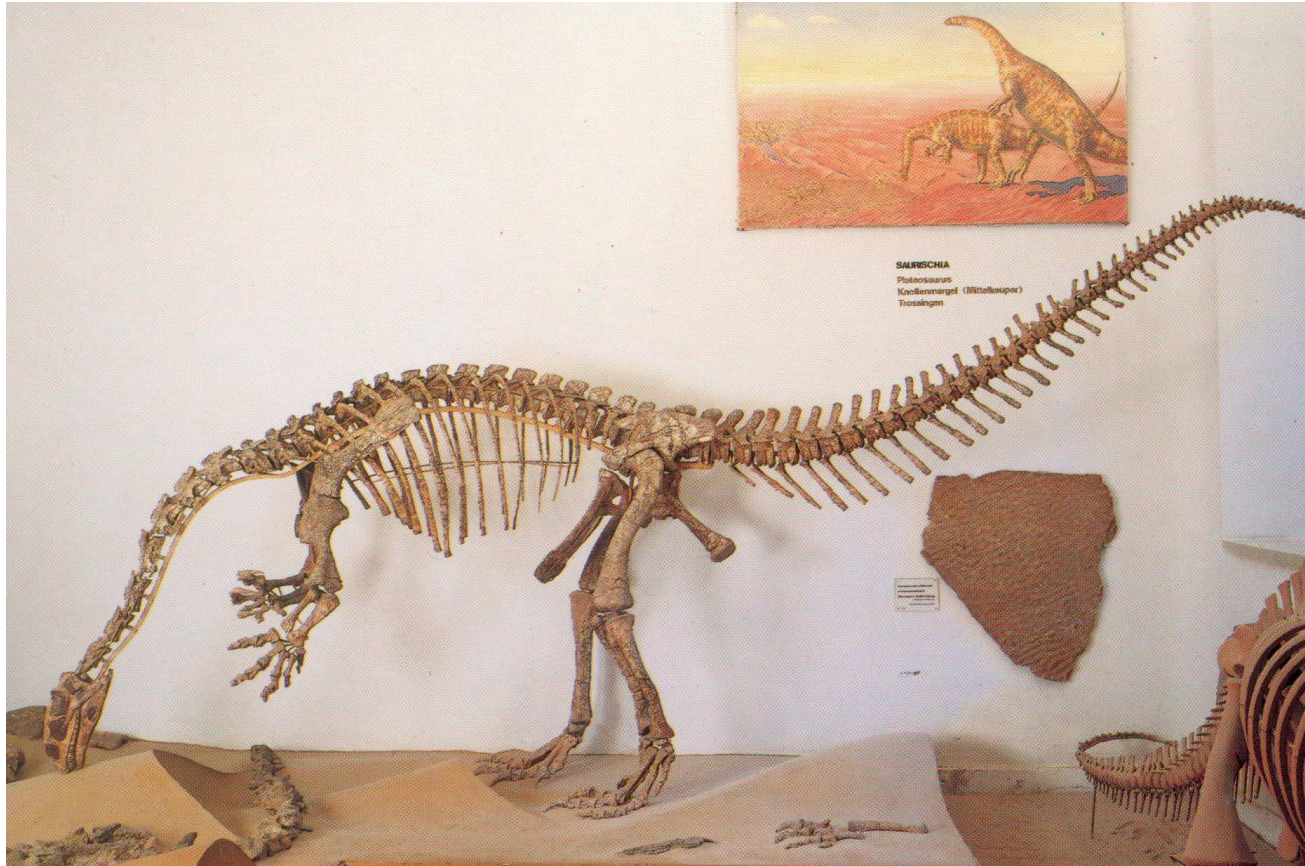


Figure 1: The mount of GPIT 1, a nearly complete individual of *Plateosaurus engelhardti* in the IFG Tübingen.

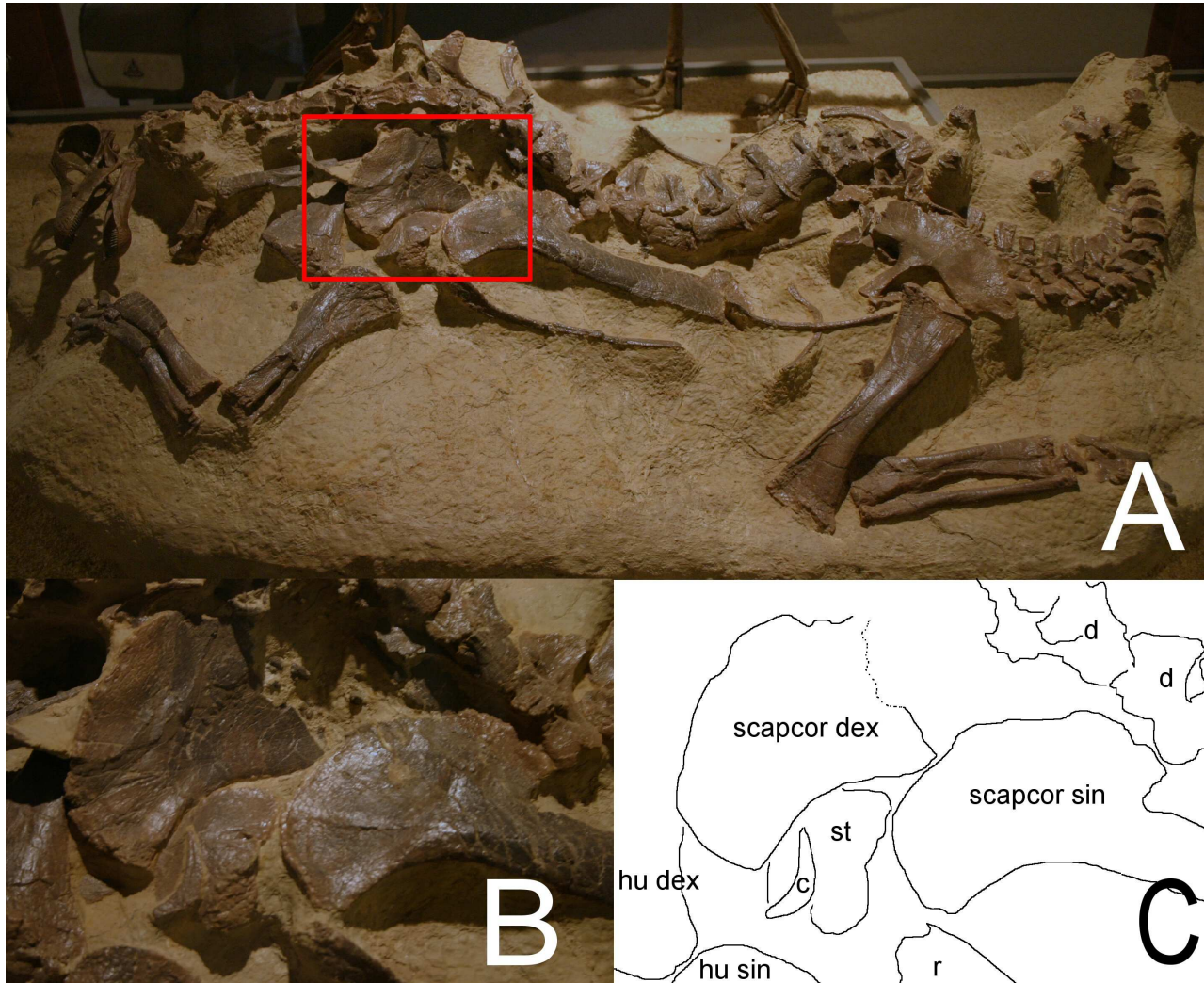


Figure 2: The skeleton of 'Tony', a baby diplodocid from the Morrison Formation of Wyoming, US (SMA unnumbered). **A:** total of the skeleton, note that the skull is a plaster model. Red rectangle marks the area enlarged in **B:** closer view of the pectoral region. **C:** outline drawing of the region shown in B. Note the fused clavicles. c = clavicles, d = dorsal vertebrae, hu dex and hu sin = dextral and sinistral humeri, scapcor dex and scapcor sin = dextral and sinistral scapulacoracoids, st = sternal

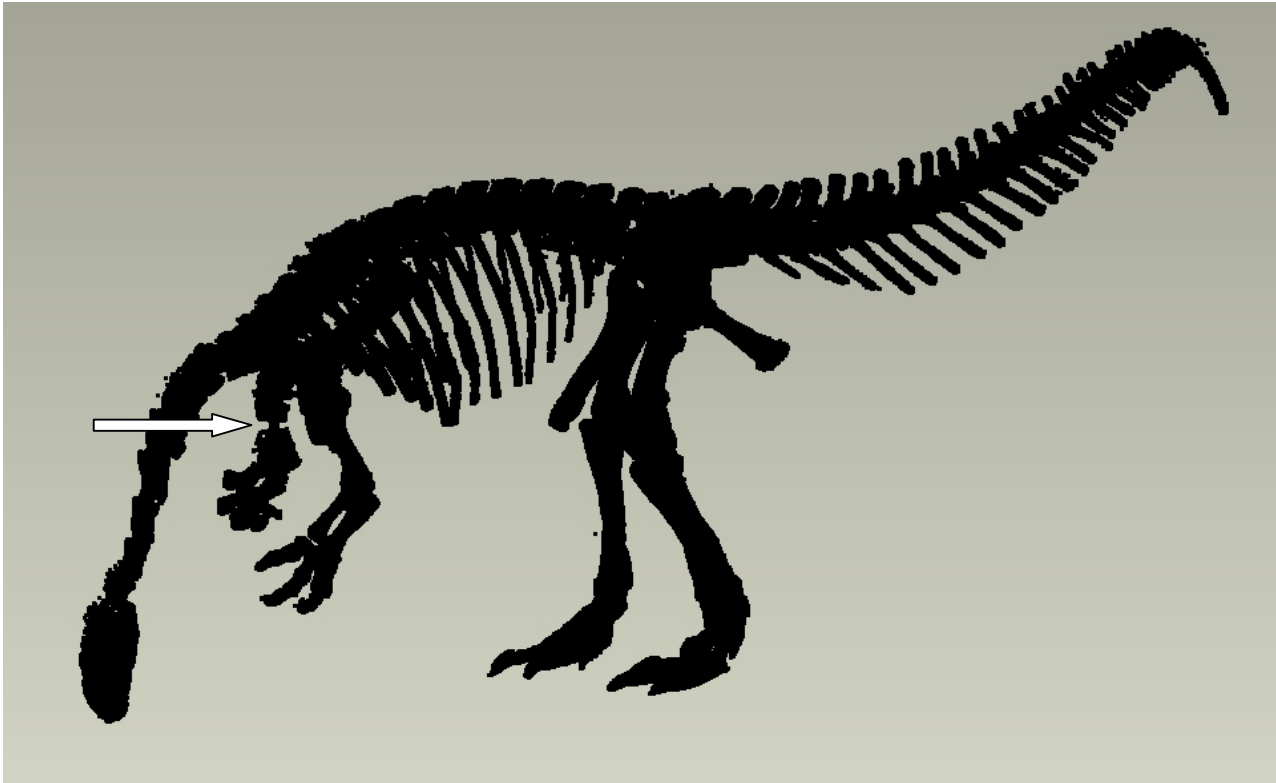


Figure 3: High resolution laser scan of *Plateosaurus engelhardti* (GPIT 1) mount in the IFGT. 3D acquired by the workgroup of H.C. Gunga. Arrow indicates visible support structure between dextral upper and lower arm.



Figure 4: A Research Casting International technician testing the fit of the iliac spike on the MNHB *Kentrosaurus* skeleton. The spike is a 3D printed copy based on a laser scan of the original bone. Note the metal armatures on the rest of the bones that were created using such 3D printed copies.



Figure 5: Ready for digitizing: the Immersion Microscribe 3D digitizer, connected to a laptop computer, set up for acquiring data of a *Diplodocus* longbone, which rests on the specially designed holder. Note the foot pedal used to control digitizer data transfer to the computer. Photo by A. Hohloch

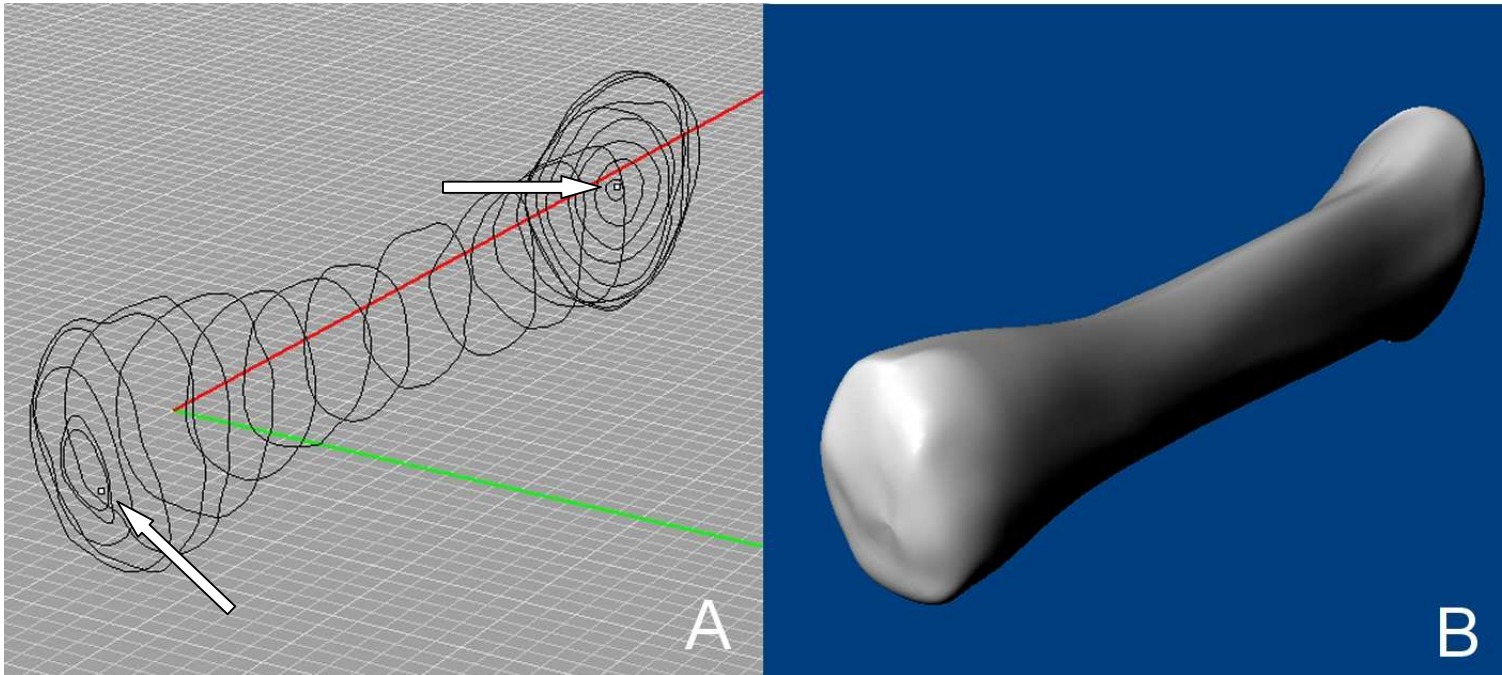


Figure 6: Digital file of the dextral Radius of *Dicraeosaurus sp.* (MNHB MB.R.2622). **A:** closed curves digitized on the specimen. Note the start and end points (arrows) for the closed loft. **B:** Lofted surface based on the curves in A.

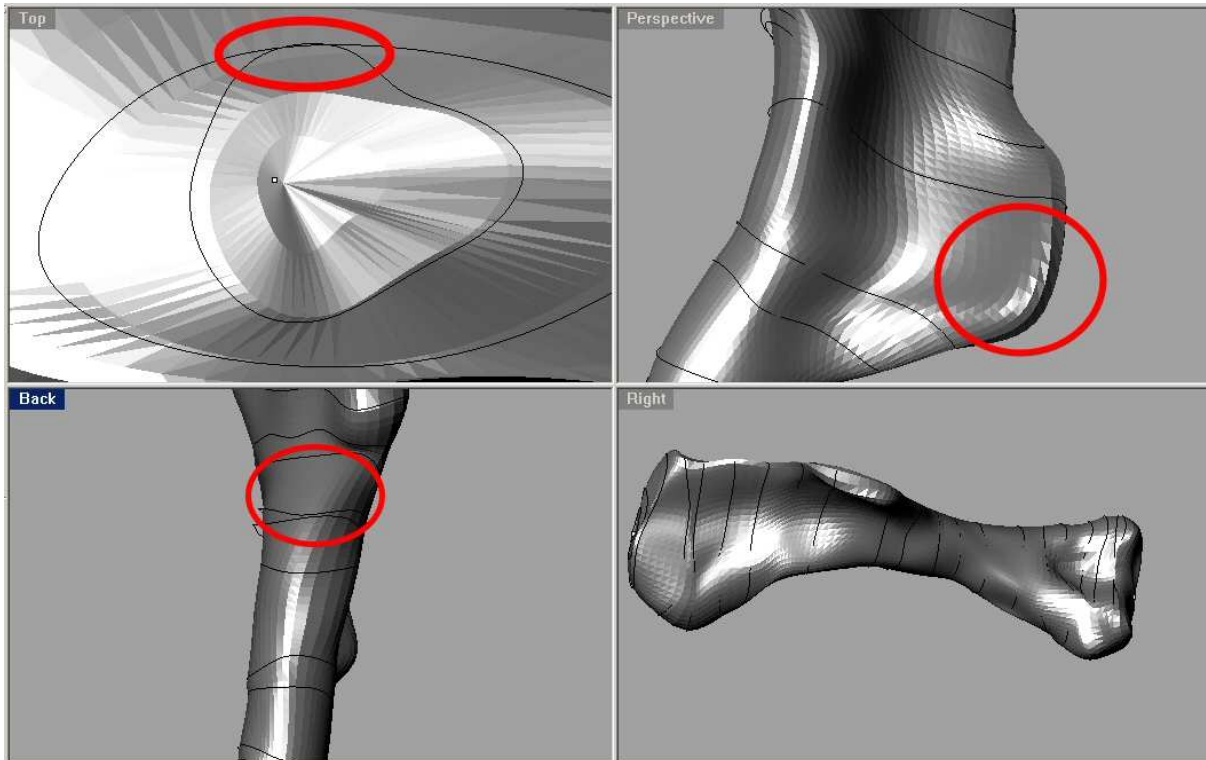


Figure 7: Examples for well placed and badly placed curves on a humerus of *Plateosaurus*, superimposed on a photograph of the specimen. Red circles show problematic areas. Top left: curves cross. Bottom left: Two curves are not subparallel. Top right: curves omit the tip of the crista. Bottom right: total view.

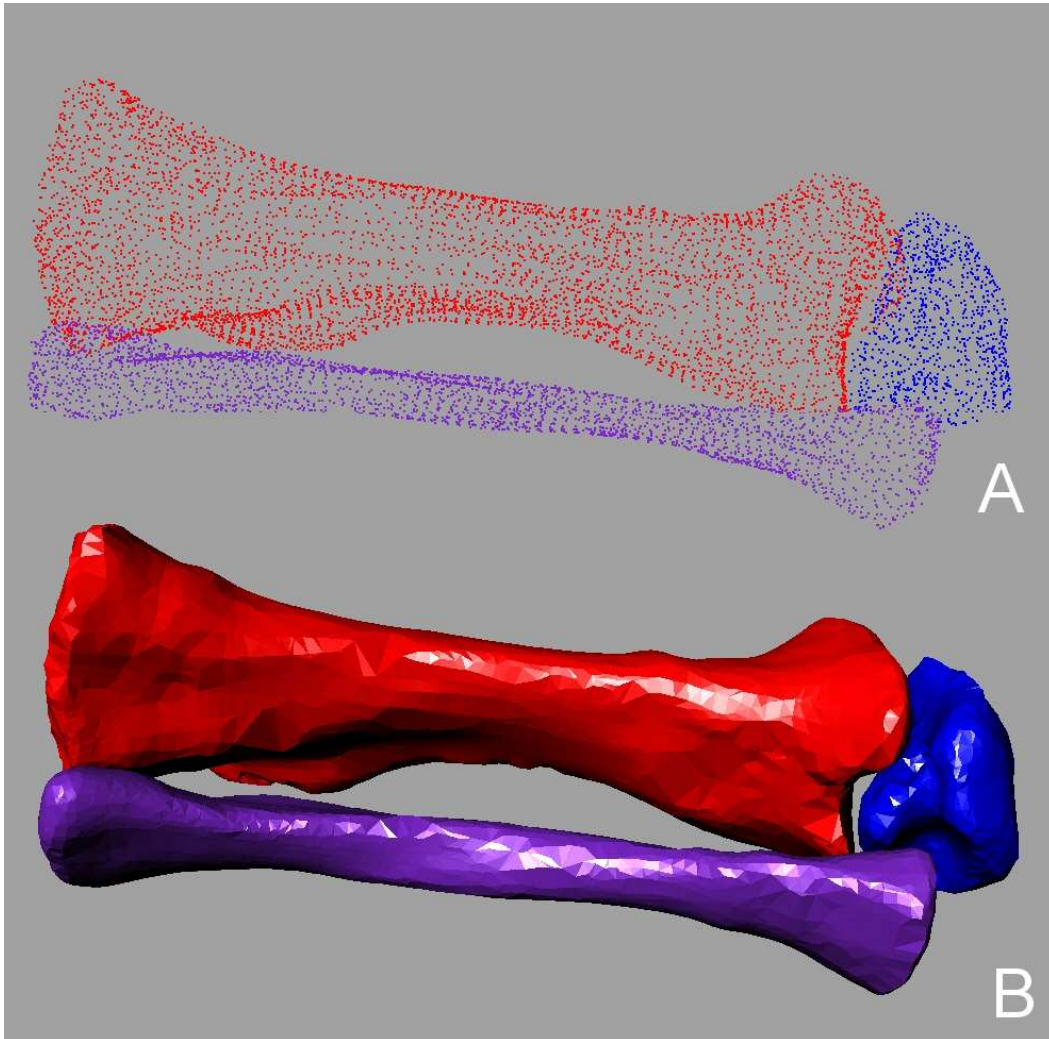


Figure 8: Sinistral Tibia, Fibula and Astragalus of the MNHB *Dicraeosaurus hansemanni* mount. These three bones were taken off the mount and digitized while still connected by metal armatures **A:** point cloud files as digitized, the color was changed to distinguish the different elements. **B:** STL polymesh files as produced from the point clouds in Geomagic 8.0®. Some editing in hardly accessible places was required.

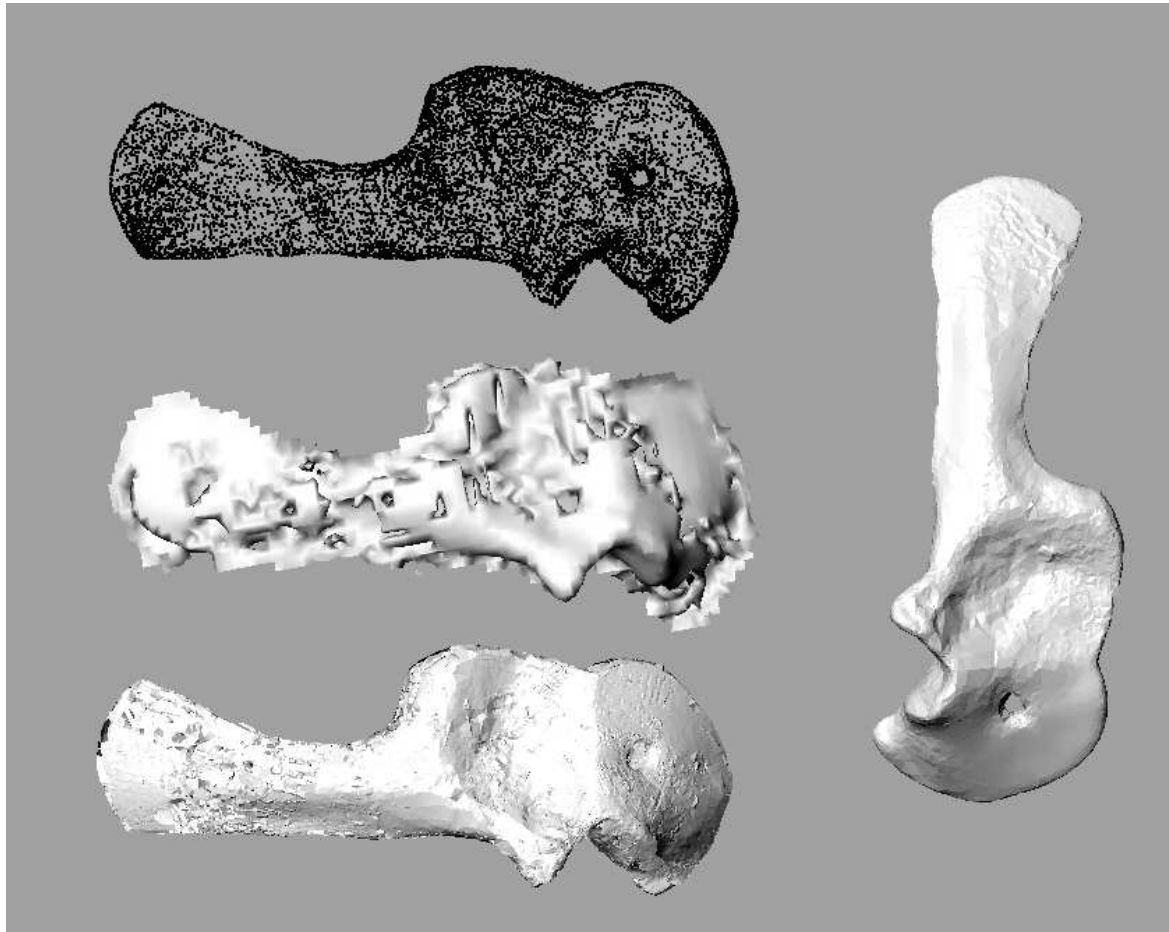


Figure 9: Dextral scapulacoracoid of *Dicraeosaurus hansemanni* (MNHB skeletal mount) meshing examples. Top left: original point cloud data, Middle left: meshed in Rhinoceros 3.0®, bottom left: meshed in Geomagic 8.0®. Note that the Geomagic 8.0® files is much smoother and has no artifacts along the margins, as opposed to the Rhinoceros 3.0® file. Right: finished file after editing, based on Geomagic 8.0® file.

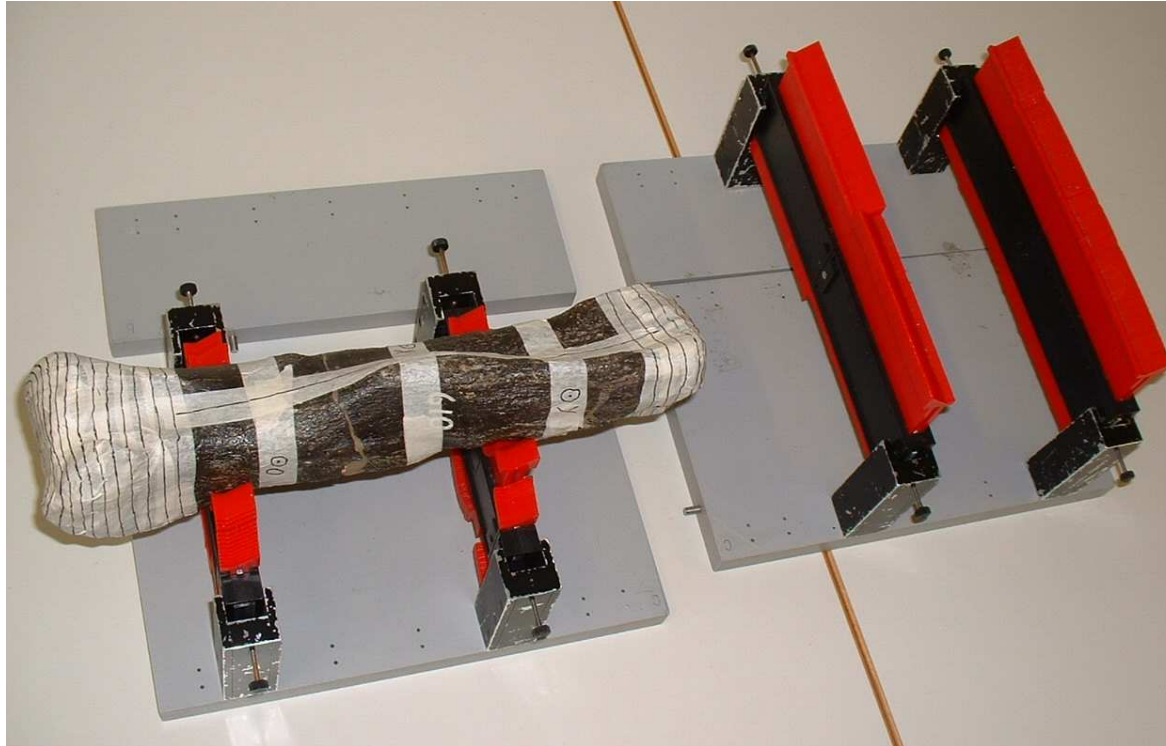


Figure 10: Detail view of the fossil holder designed for this project: on the left, the holder in minimum configuration carries a *Diplodocus* metacarpal from IFGT marked for NURBS digitizing, top and right are the extension parts for larger specimens. Note that the width of the contour gauges can be doubled for broad specimens. Photo by A. Hohloch

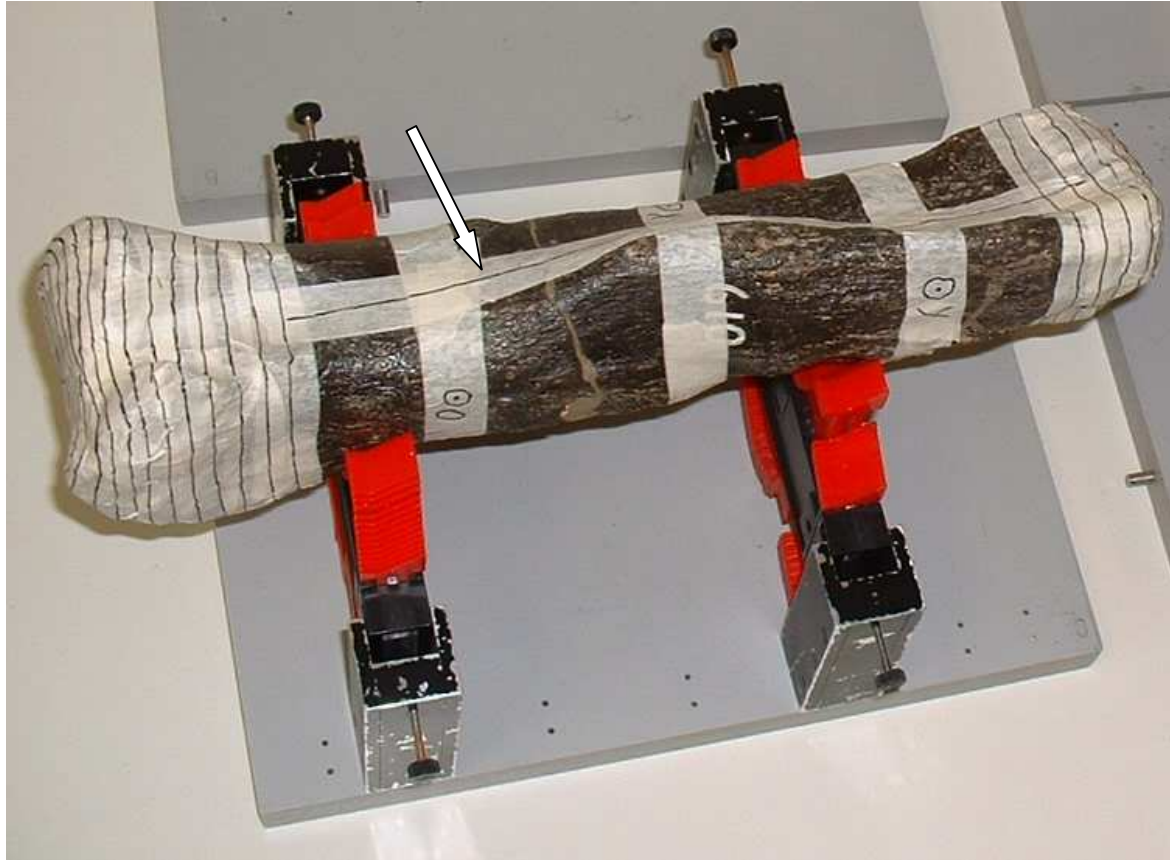


Figure 11: A closer view of the *Diplodocus* metacarpal prepared for closed curve digitizing. Note the three coordinates marked by a circled dot and a letter (o = origin, x = x-axis, y = y-axis). The line running the length of the bone indicated by the arrow is the seam line; to display it, the bone has been turned upside down. Near the articular ends, curves have been marked on tape to make digitizing easier. Photo by A. Hohloch.

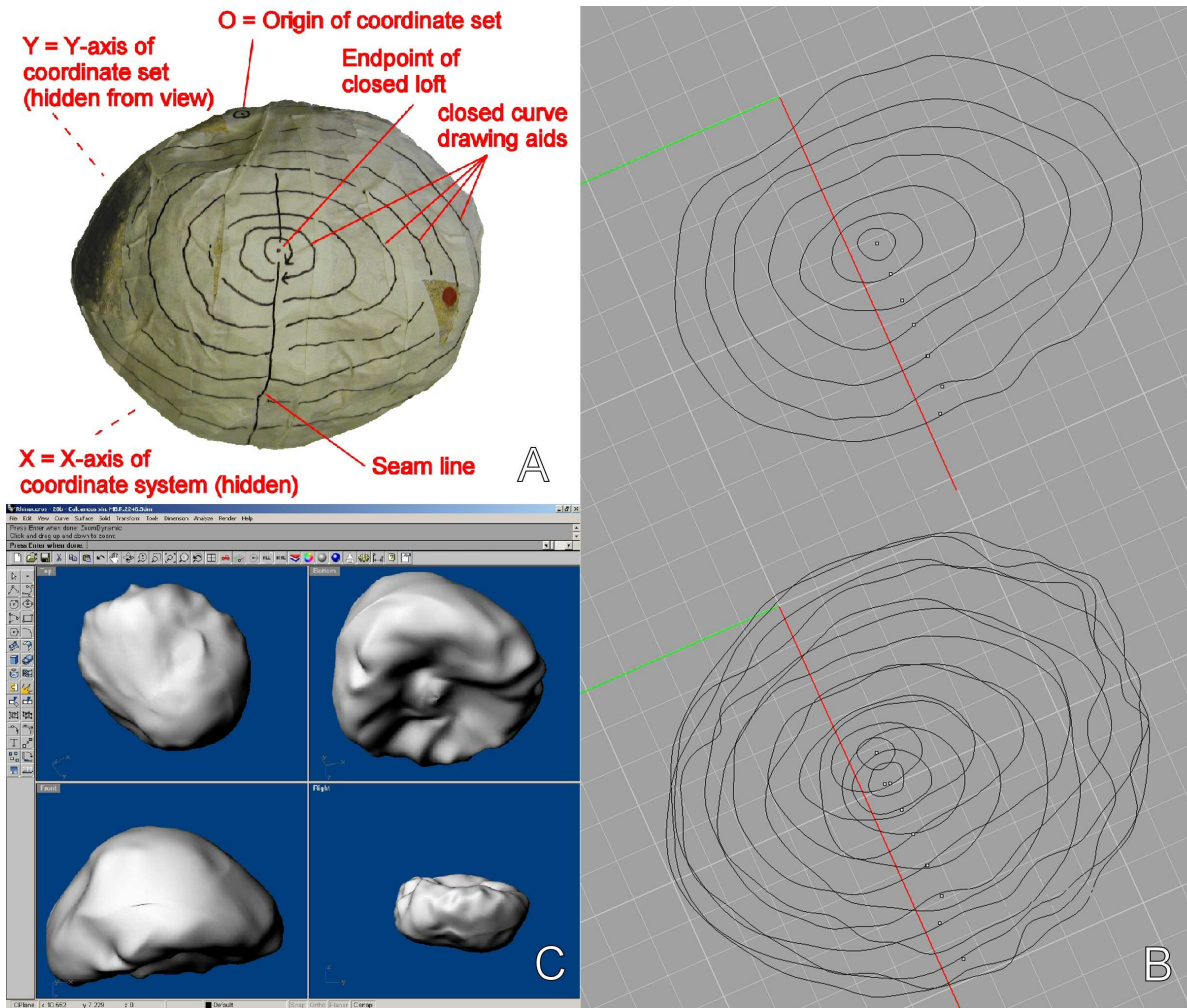


Figure 12: Sinistral calcaneum of *Brachiosaurus brancai* (MNHB, MB.R.2246. **A:** the specimen prepared for digitizing, not the seam line, the marked curves and curve directions and the position of the coordinates along a horizontal plane that is accessible also if the bone is turned upside down. **B:** closed curves digitized in Rhinoceros 3.0®, top shows curves of one side, bottom shows combined curves from both sides. **C:** four views of the lofted surface in Rhinoceros 3.0® render preview.

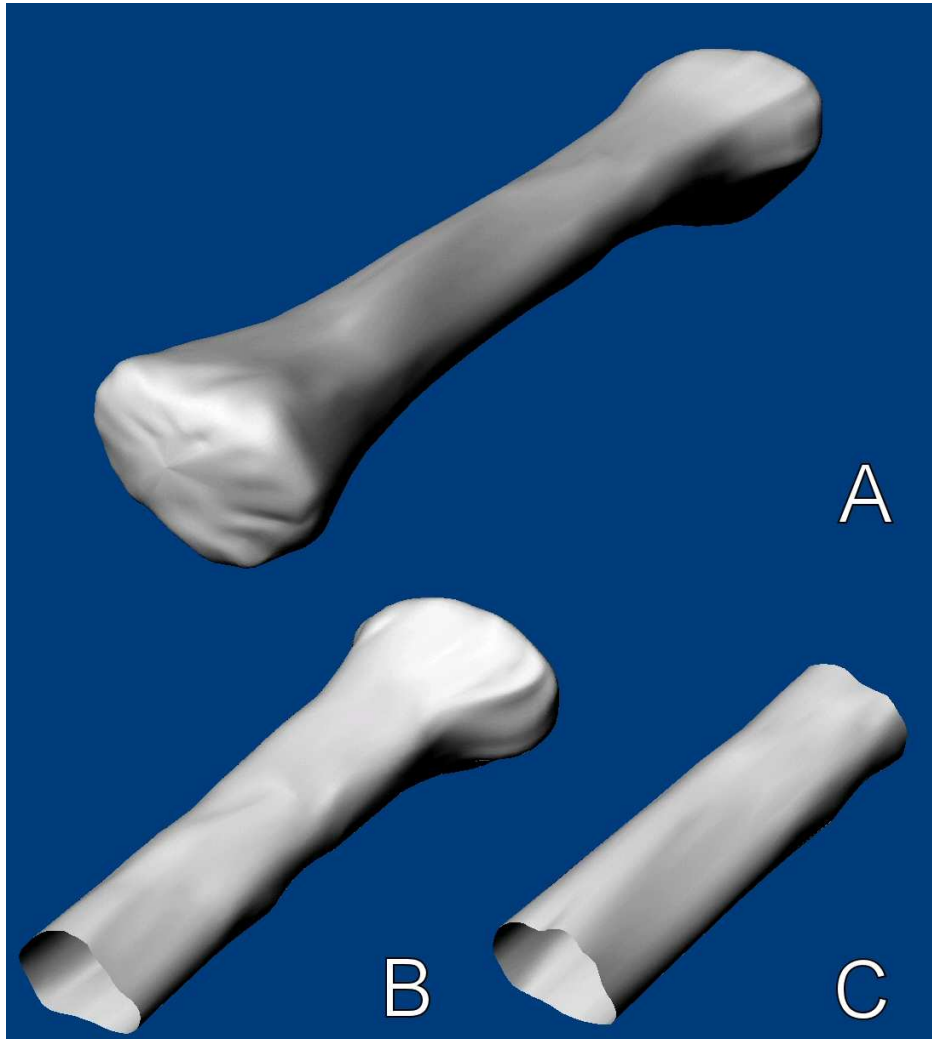


Figure 13: Examples of open and closed lofts. **A:** complete closed loft of a dextral radius of *Brachiosaurus brancai* (MNHB MB.R.2687). This loft uses closed curves and two endpoints **B:** partial loft of the same specimen using closed curves and only one endpoint. This loft is open on one end. **C:** partial loft using only curves; it is open on both ends.

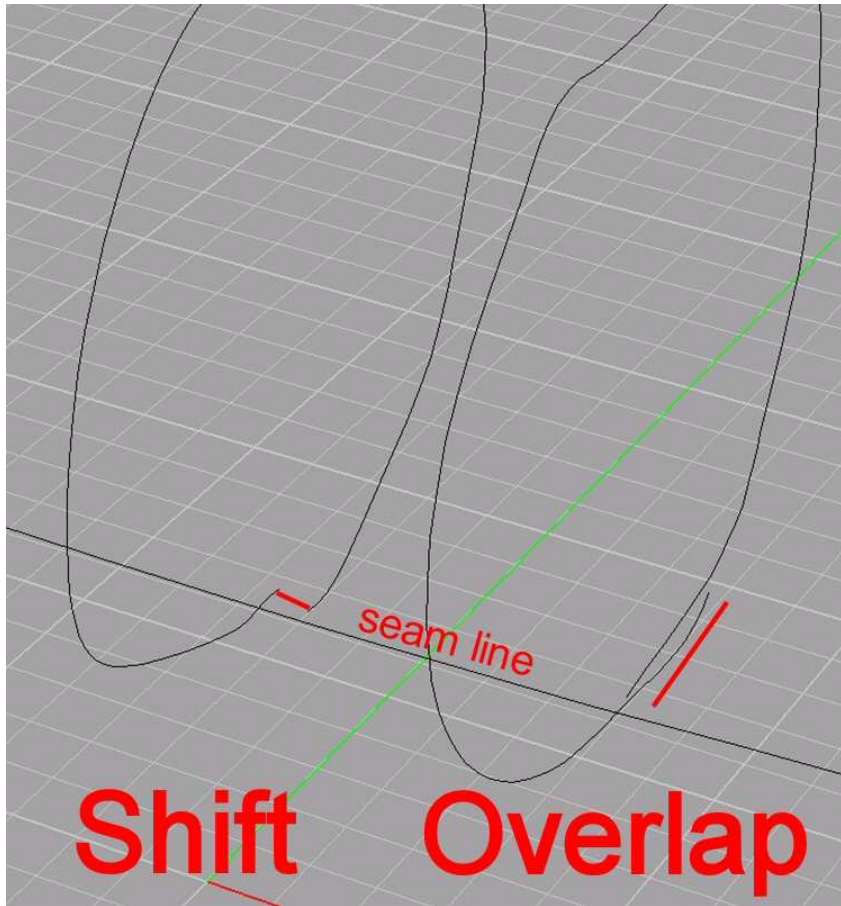


Figure 14: Shift and overlap in open curves; in closed curves this would lead to artifacts along the red markings.

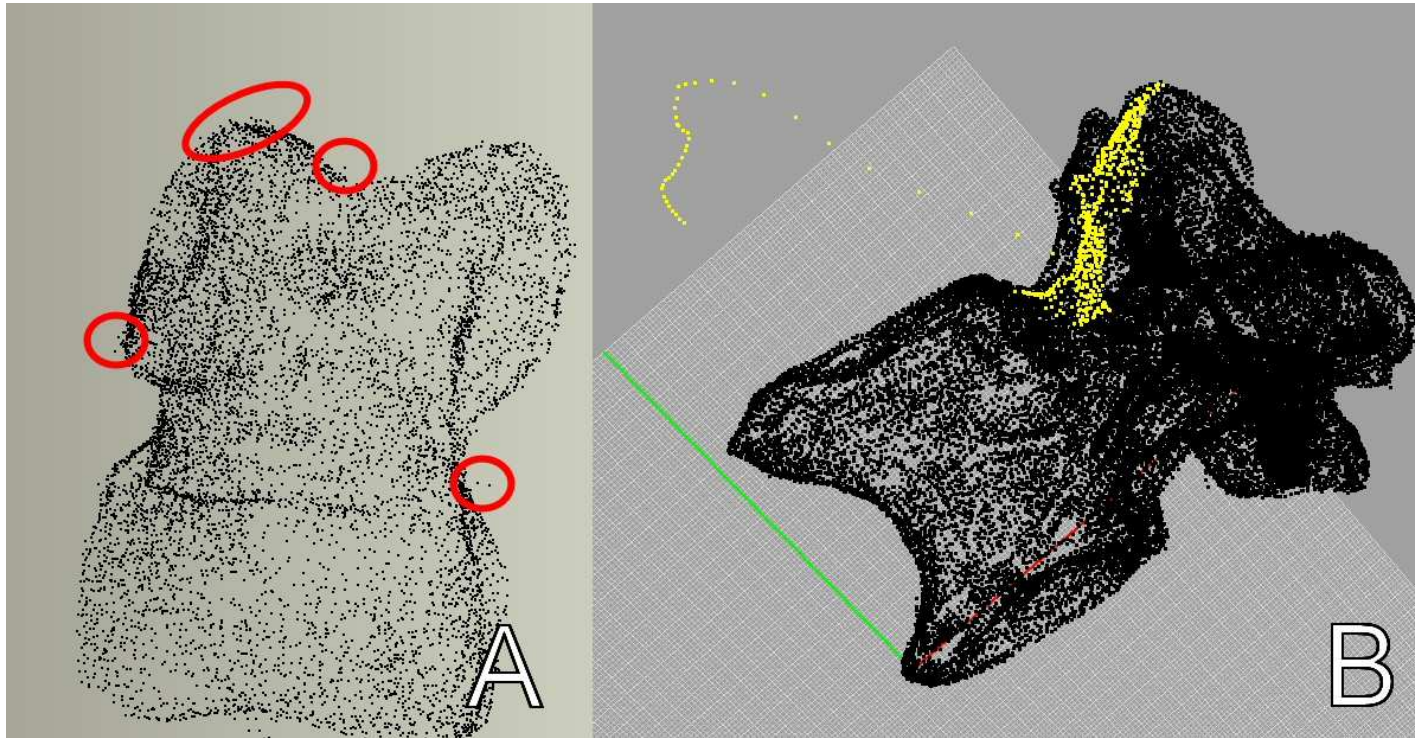


Figure 15: *Plateosaurus engelhardti* (GPIT 2) point cloud files. **A:** pedal phalanx II-1. Erroneous points visible in this view are circled in red. **B:** Dorsal 2. The point cloud with errors, marked in yellow, is easily spotted by its 'tail'.



Figure 16: Digitizing a *Diplodocus* radius (IFG exhibition mount) by leaning it against the wall with a spacer and digitizing closed curves. Note the two coordinates (arrows) of the coordinate system placed centrally on the shaft to allow easy reach independent of which end of the bone is currently 'up'.

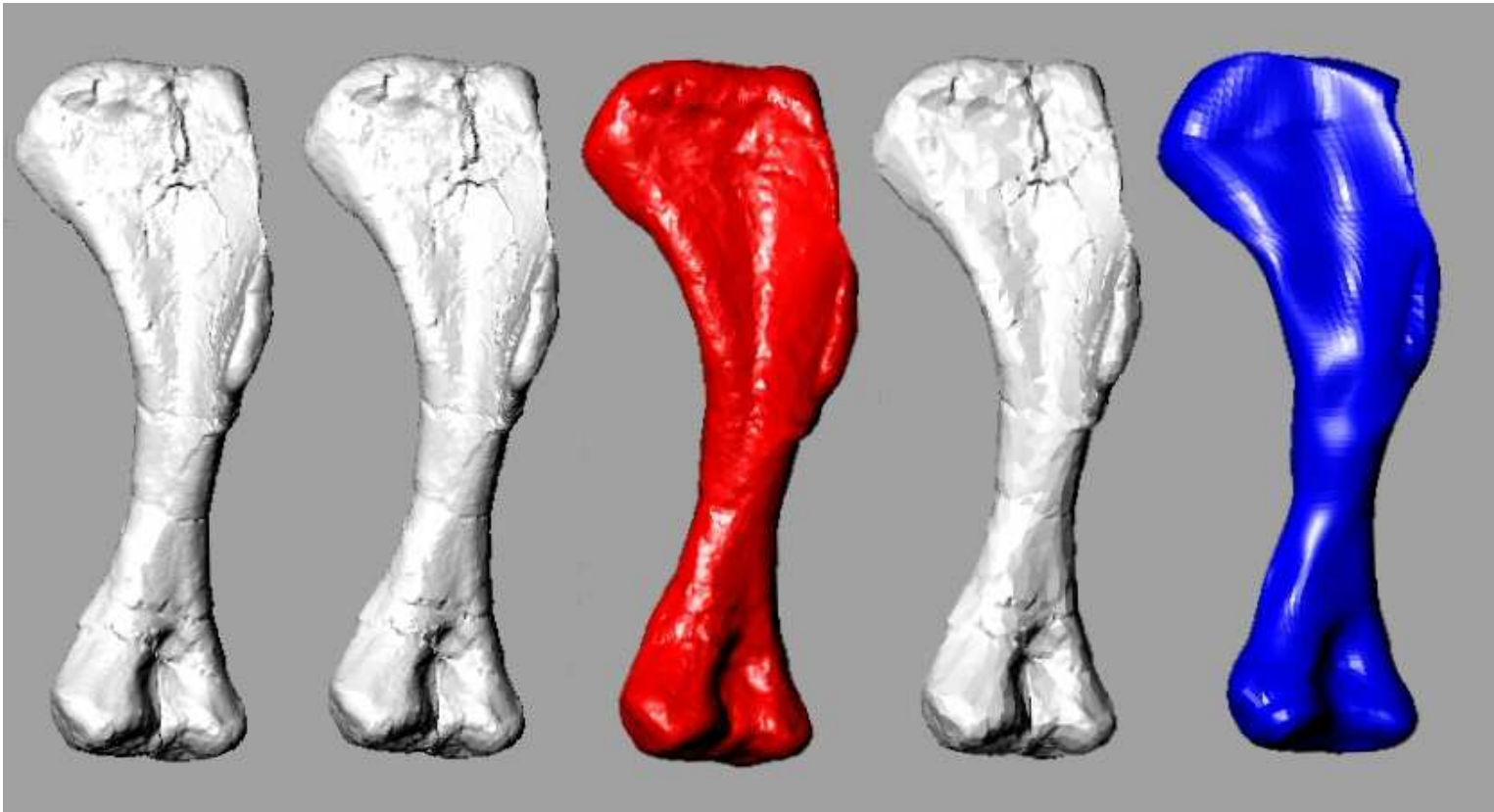


Figure 17: 3D files of the sinistral humerus of GPIT 2. Left to right: CT full scale, CT medium size, point cloud medium size (red), CT small size, NURBS curve (blue).

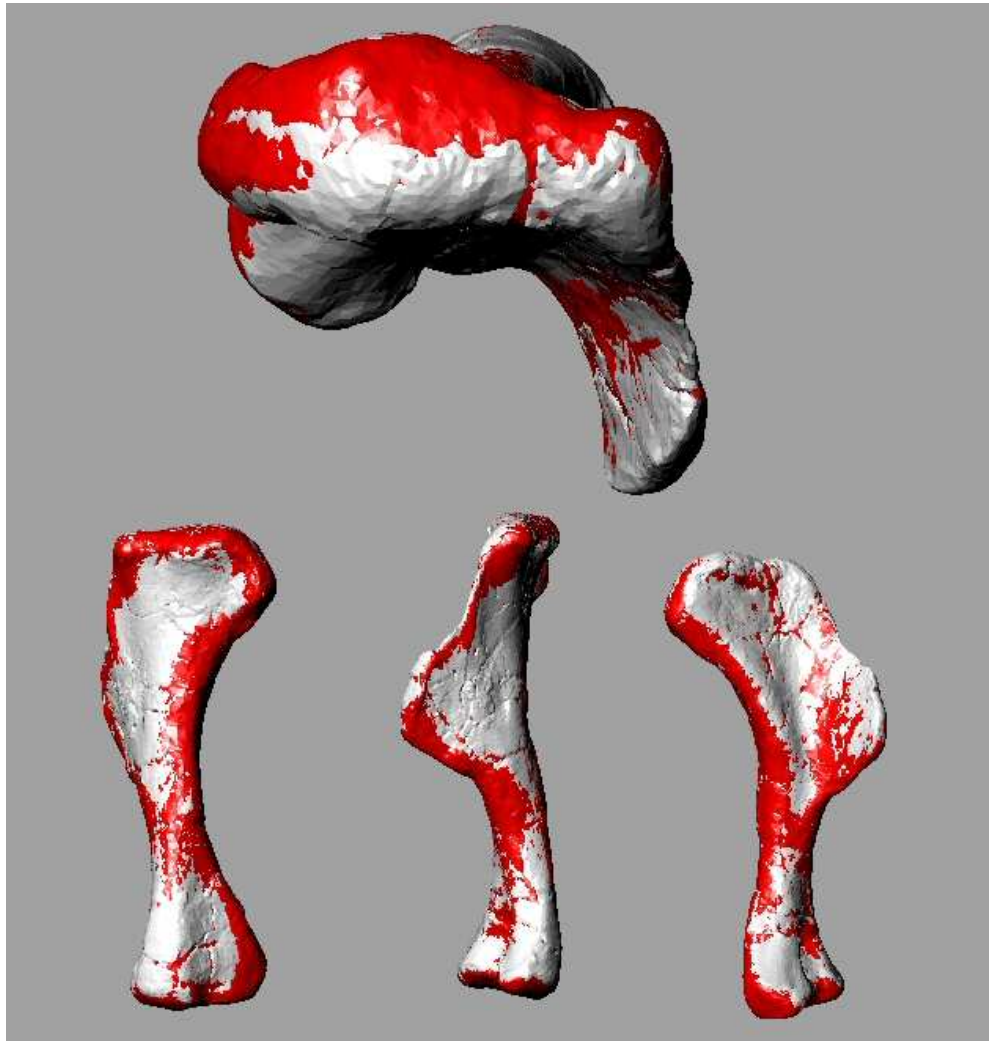


Figure 18: Superimposed views of the sinistral humerus of GPIT 2. CT based file (grey) and point cloud based file (red) of equal file size are shown in proximal view (top), posterolateral view (bottom left), lateral view (bottom middle) and anteromedial view (bottom right). Note the 'splotchy' appearance indicating only minimal differences.

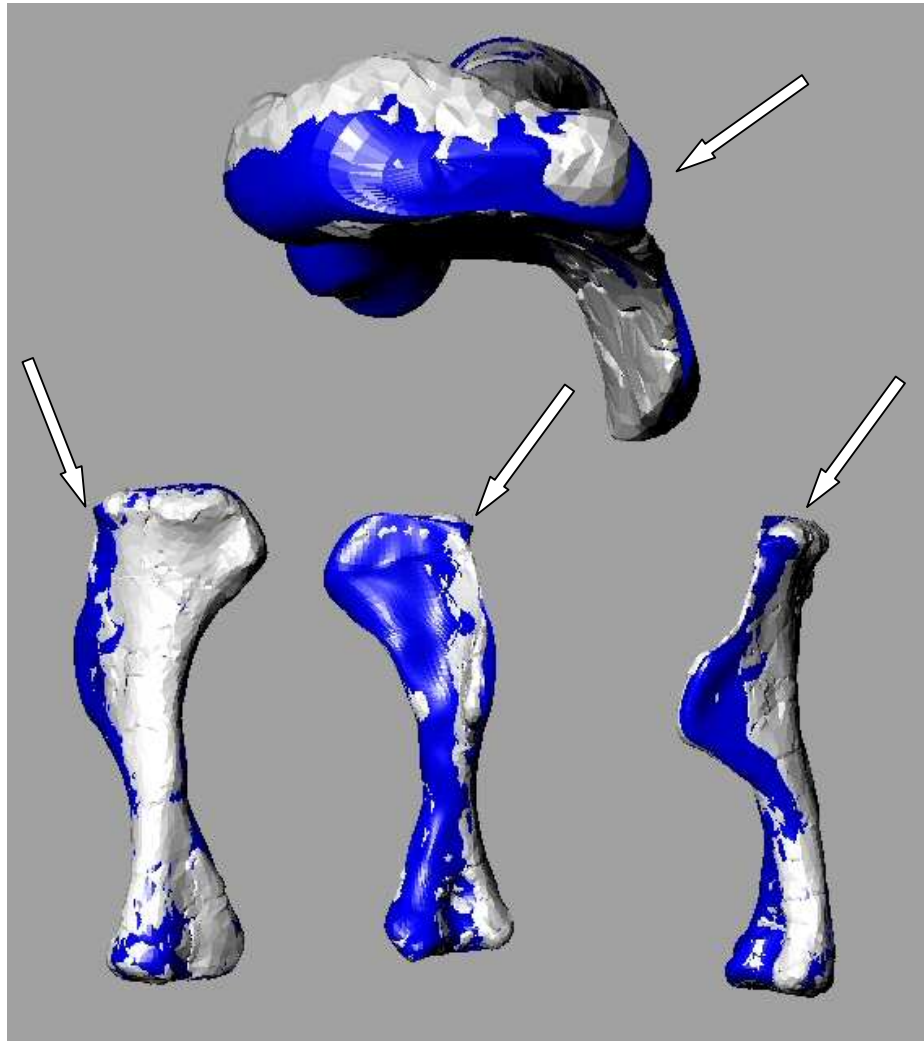


Figure 19: Superimposed views of the sinistral humerus of GPIT 2. CT based file (grey) and NURBS based file (red) of equal file size are shown in proximal view (top), posterolateral view (bottom left), lateral view (bottom middle) and anteromedial view (bottom right). Note large areas of single color indicating larger differences than evident in Figure 18 for the CT and point cloud files. Arrows indicate significant inaccuracy in NURBS file on articular end.

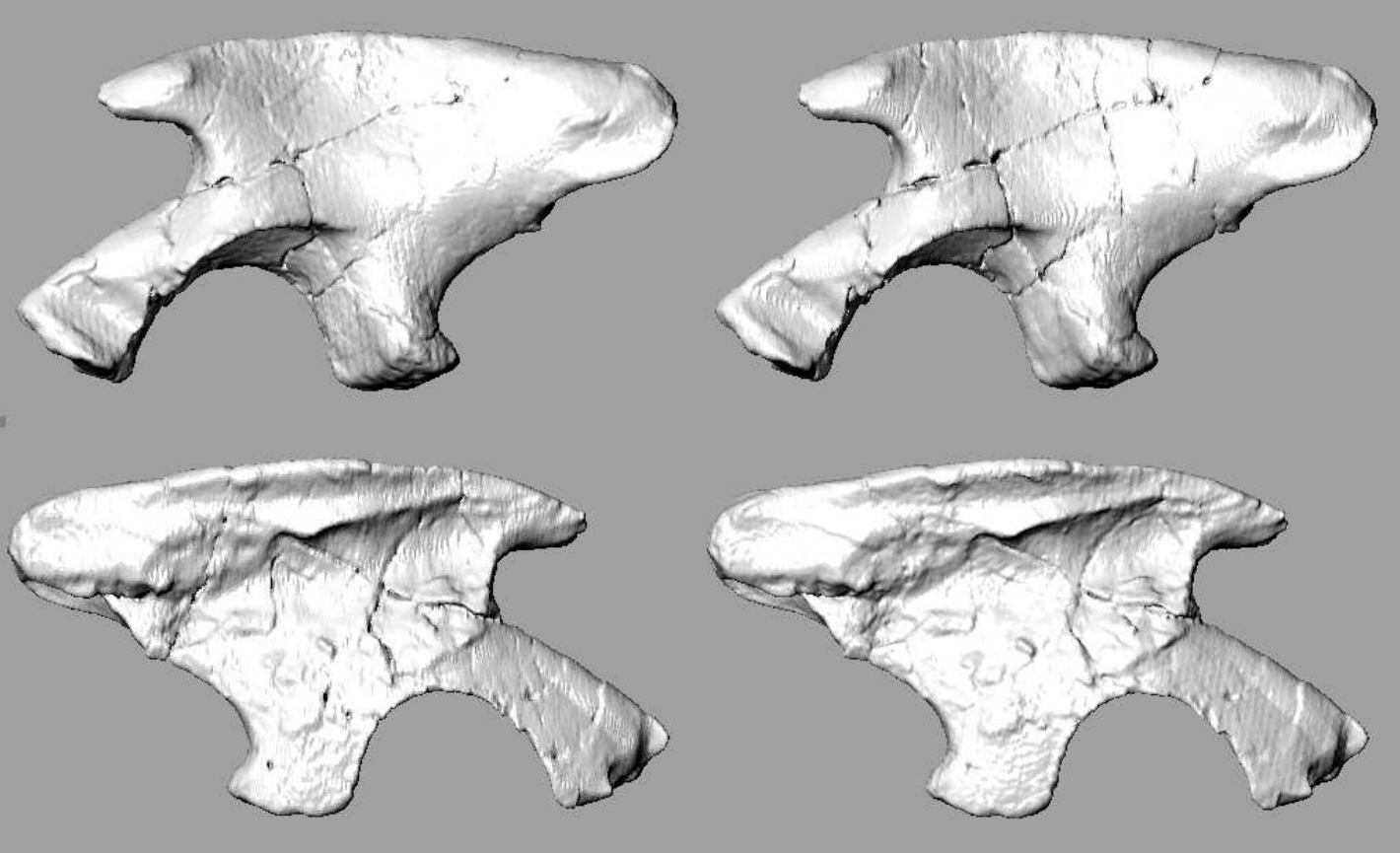


Figure 20: Comparison of full size (top left and bottom right) CT based file and reduced size CT based file of the sinistral ilium of GPIT 1.

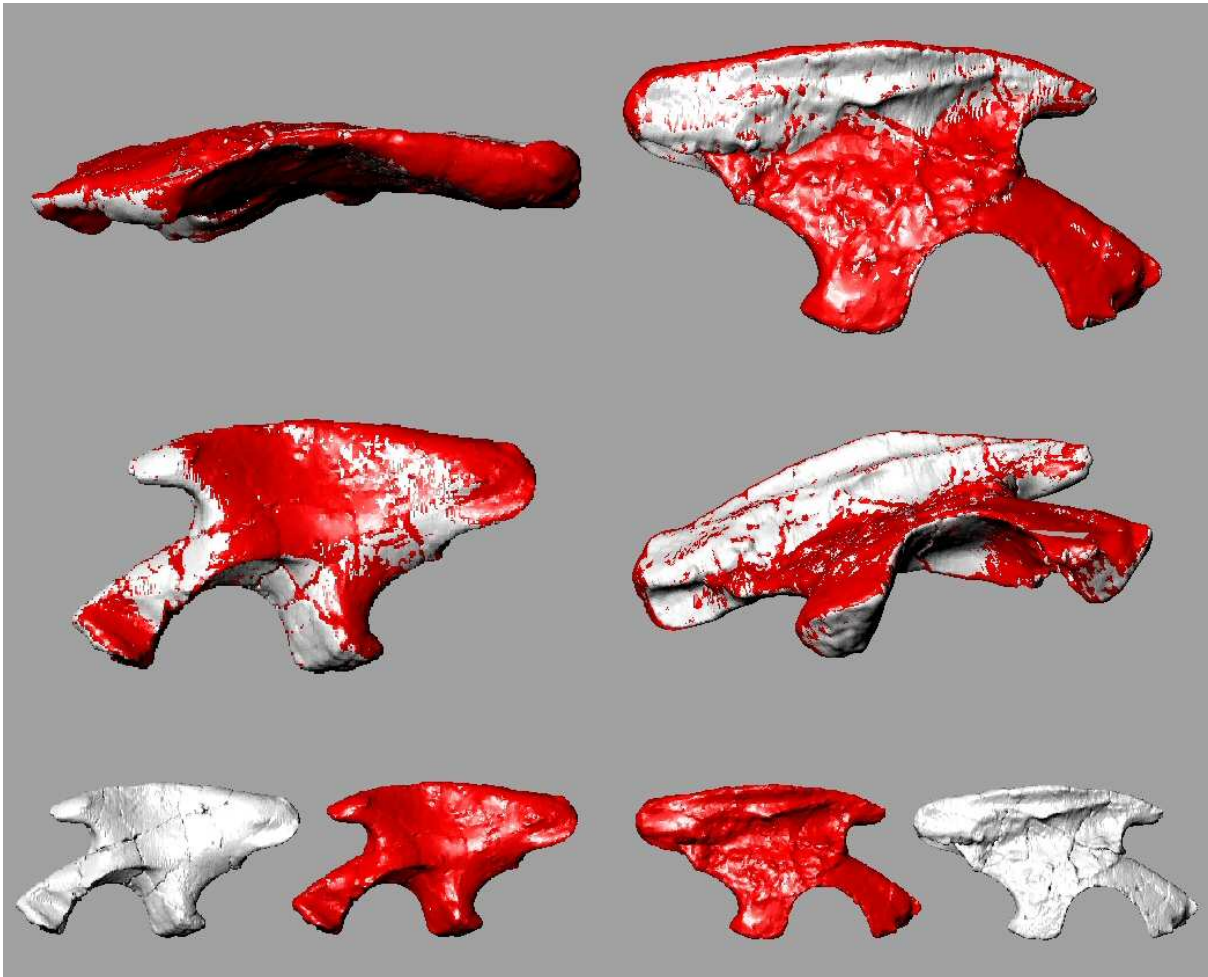


Figure 21: Comparison of CT based (grey) and point cloud based (red) digital surfaces of the sinistral ilium of GPIT 1. Superimposed files in dorsal view (top left), medial view (top right), lateral view (middle left), medioventral view (middle right). Bottom row shows the files in lateral and medial views side by side.

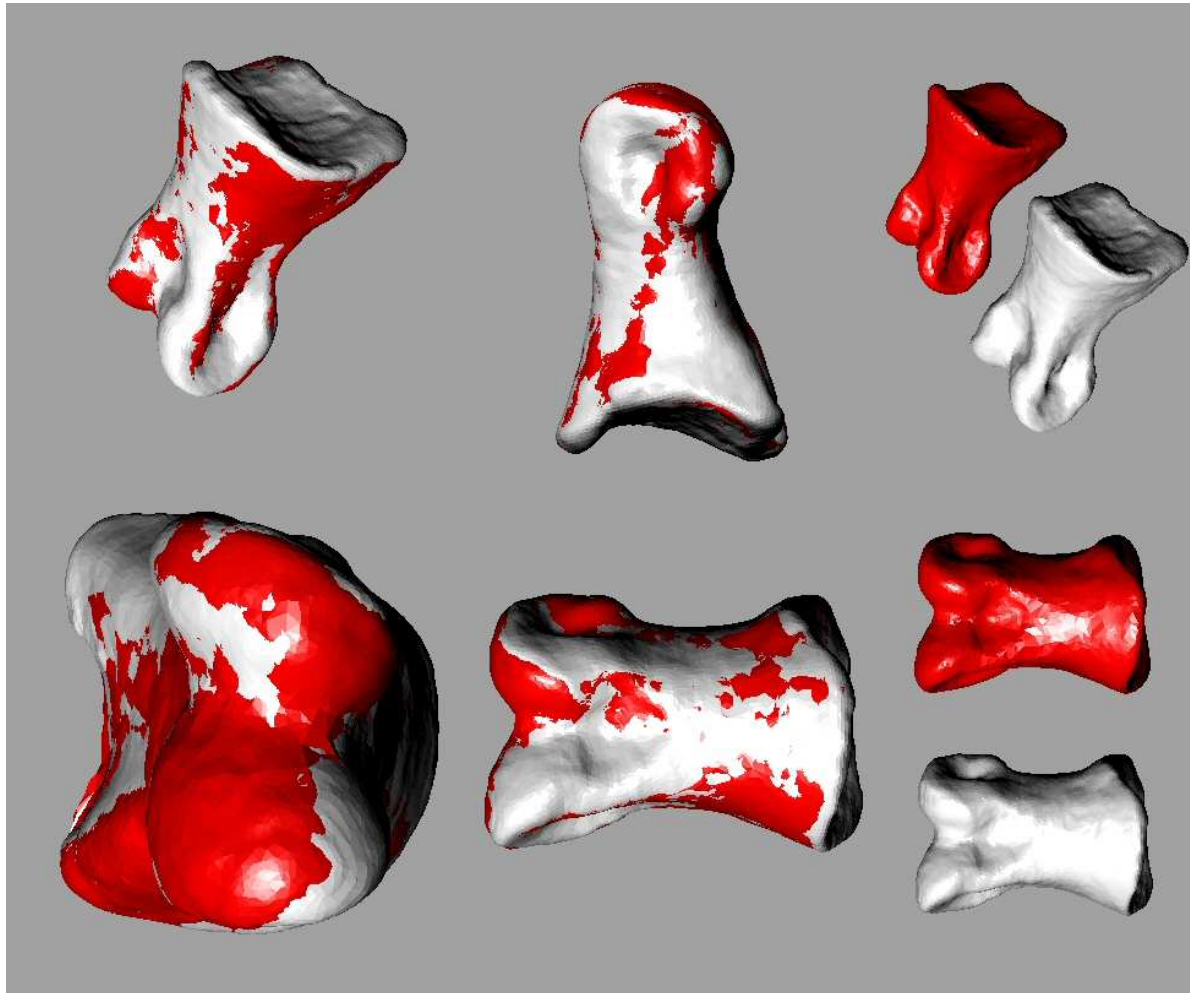


Figure 22: Comparison of CT based (grey) and point cloud based (red) digital surfaces of the sinistral pedal phalanx of GPIT 1. Superimposed files in oblique (top left); medial (top middle), anterior (bottom left) and dorsal (bottom middle) views. Right column shows the files in oblique and dorsal views side by side.

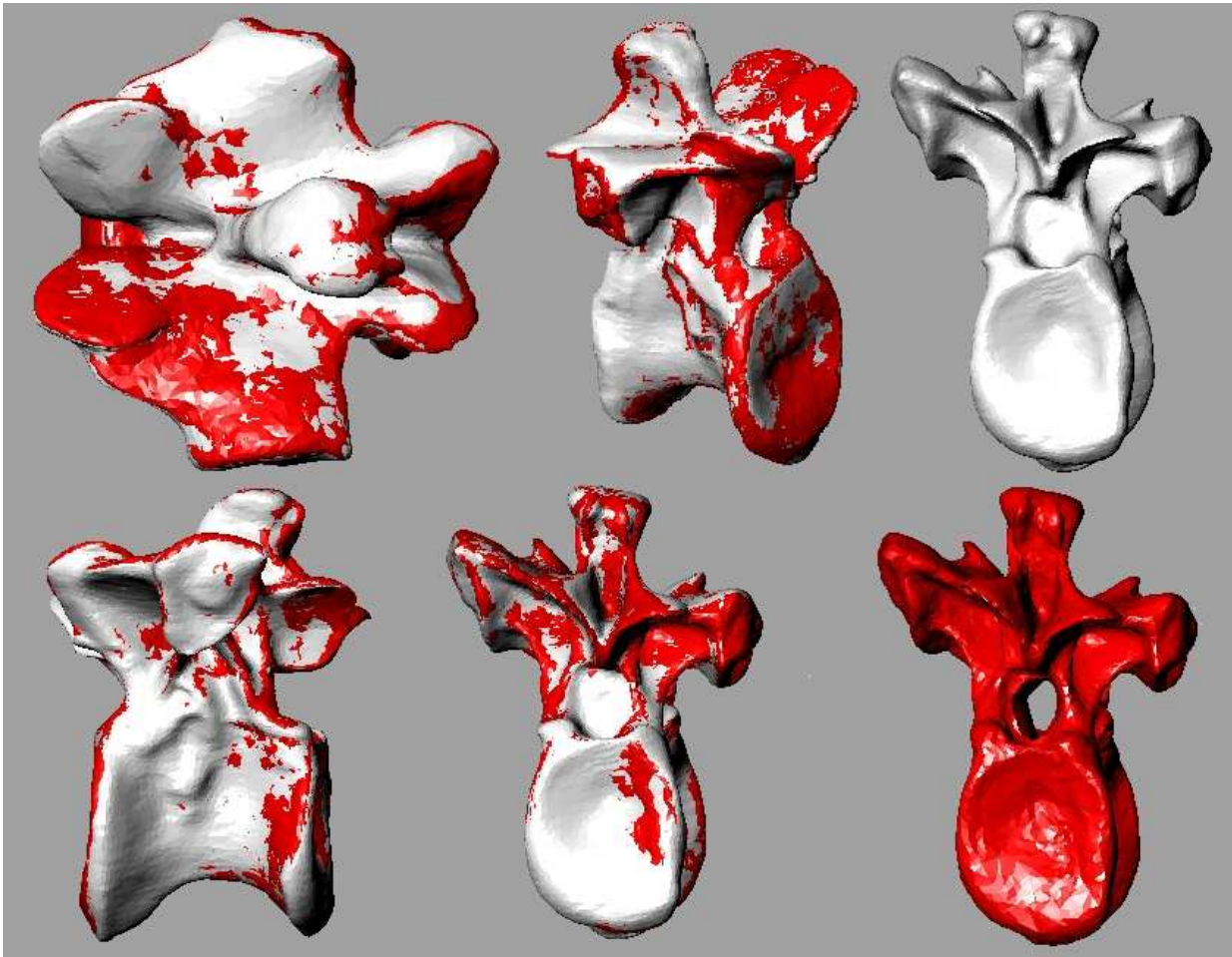


Figure 23: Comparison of CT based (grey) and point cloud based (red) digital surfaces of dorsal 2 of GPIT 1. Superimposed files in dorsal (top left); oblique (top middle), lateral (bottom left) and posterior (bottom middle) views. Right column shows the files separately in posterior view.

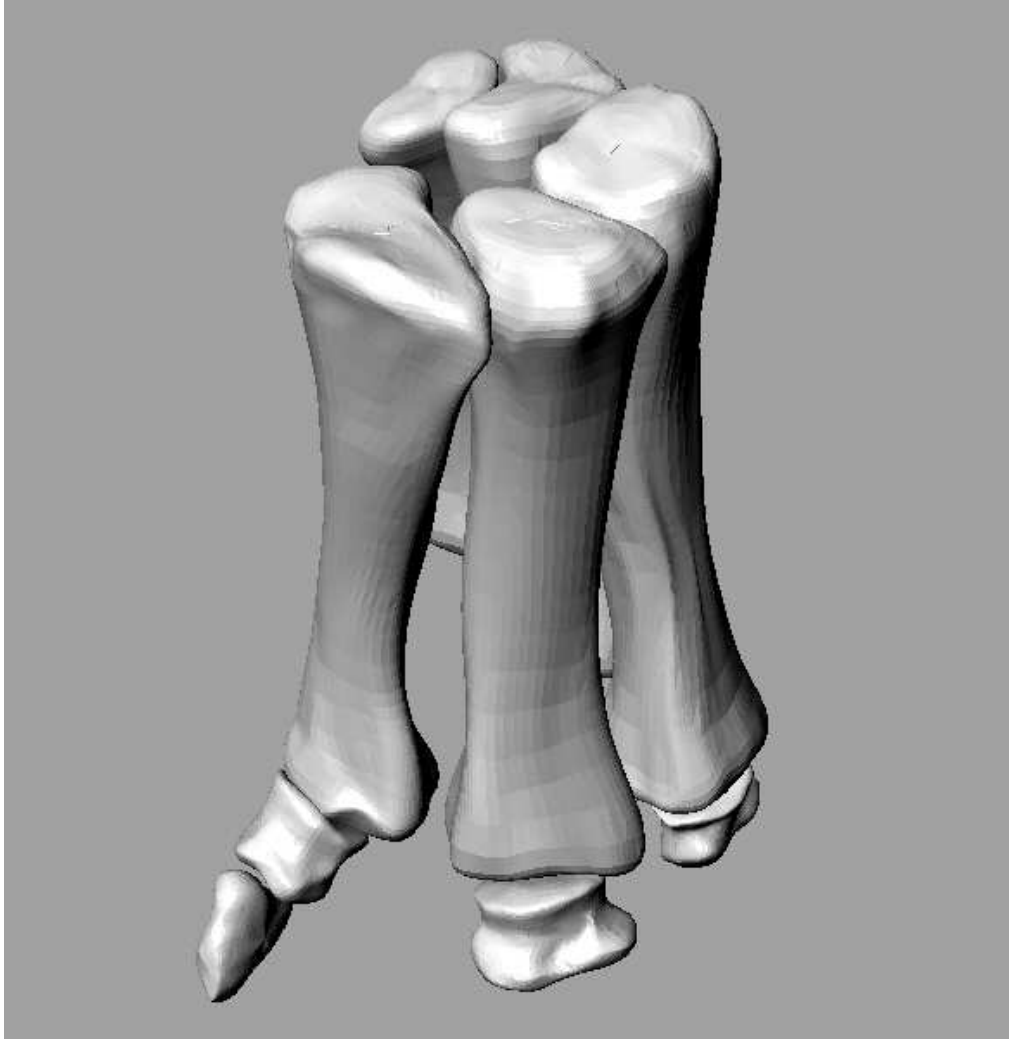


Figure 24: Oblique view of the digitally articulated sinistral manus of *Brachiosaurus brancai* (MNHB MB.R.2249 R 8 through 14). NURBS based files were used to create accurate but low resolution STL files.

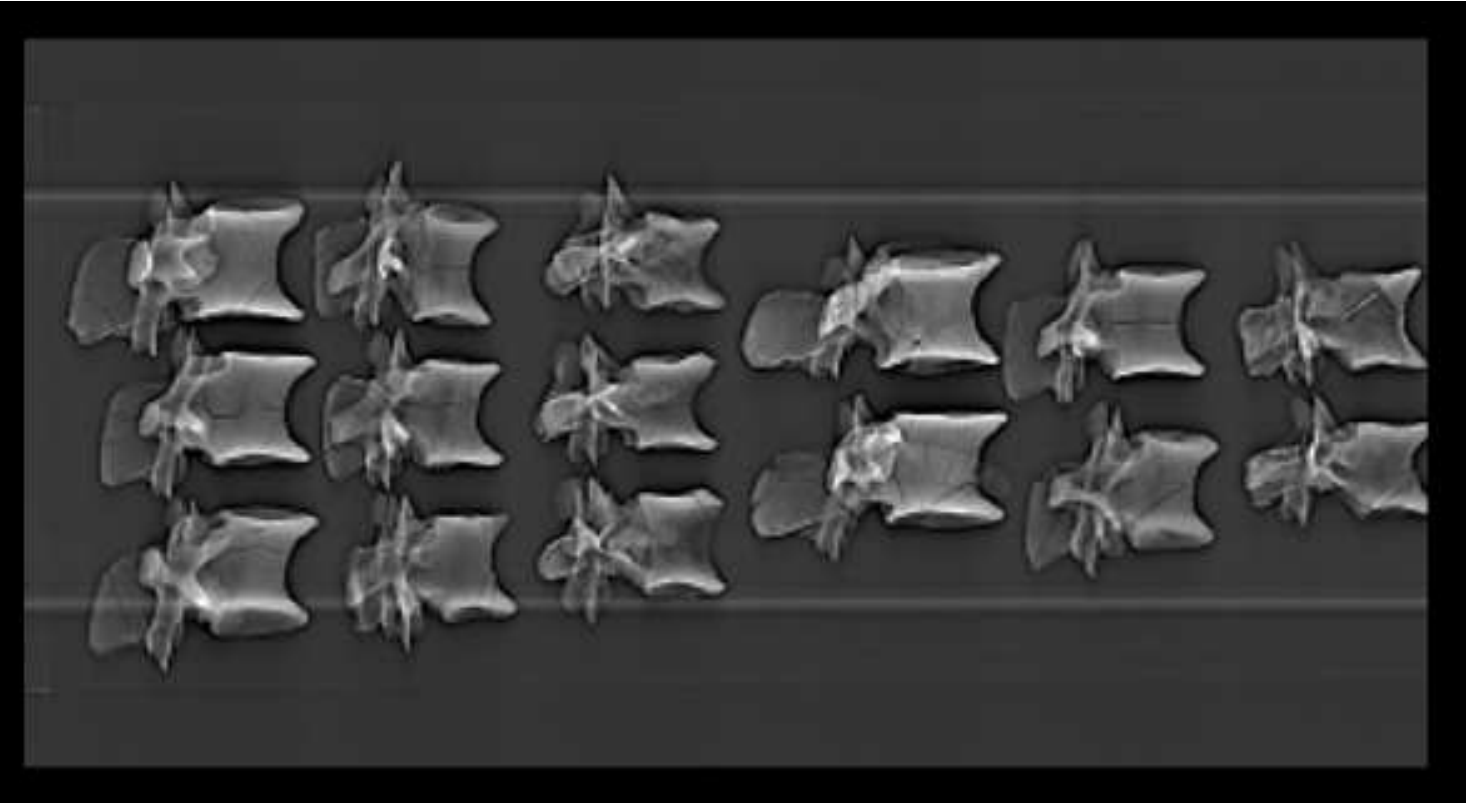


Figure 25: A topograph view of a CT scan of 15 dorsal vertebrae of GPIT 1

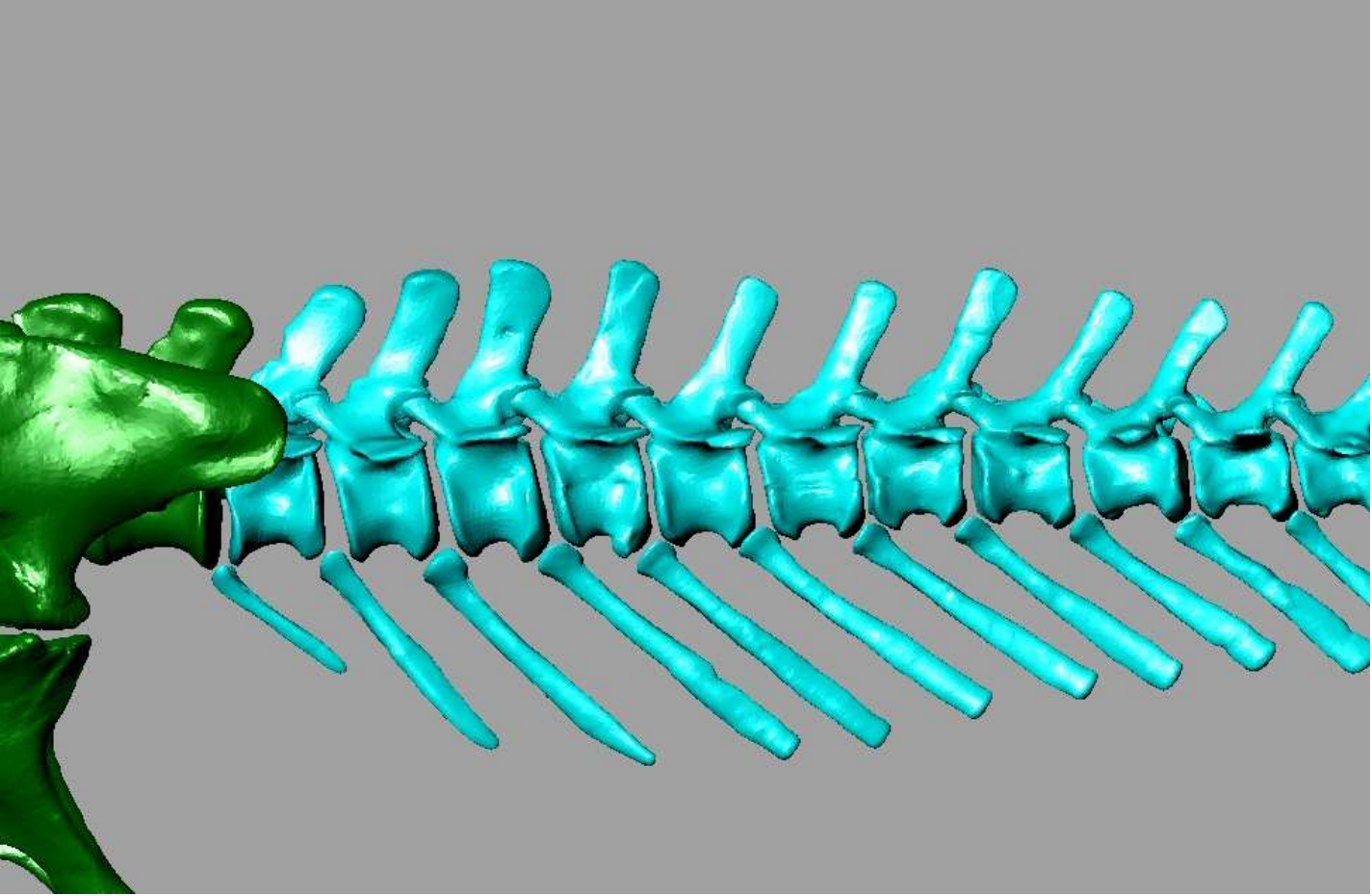


Figure 26: Anterior tail of GPIT 1 virtual skeleton in lateral view.



Figure 27: Pelvic girdle and femora of the virtual skeleton of GPIT 1 in lateral view. Note that femoral position does not utilize the full range of protraction and retraction possible.

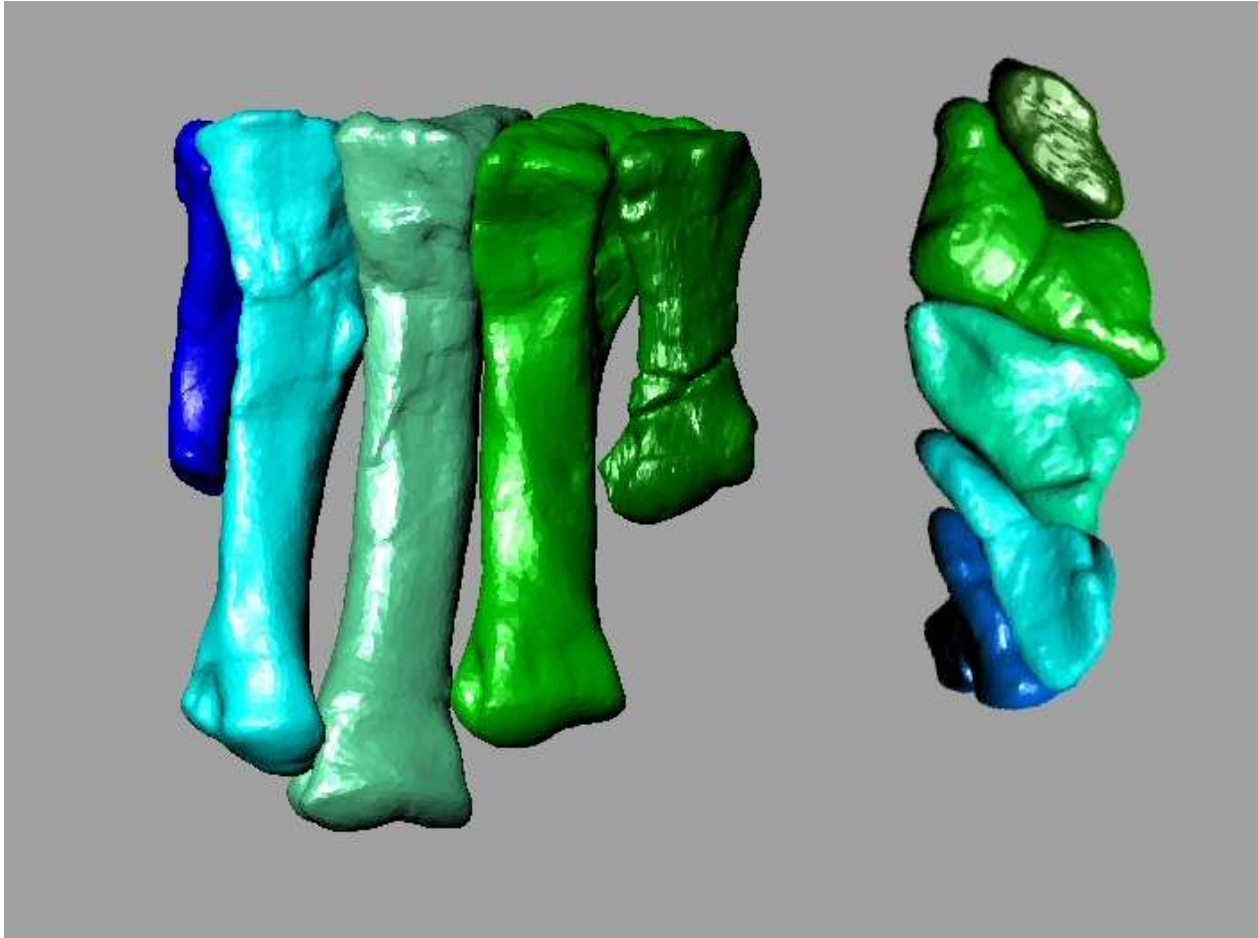


Figure 28: Dextral metatarsus of GPIT 1 virtual skeleton in dorsal (left) and proximal (right) view. MT 1 is to the right / at top.



Figure 29: Sagittal section of the forefoot of a juvenile elephant (ZST unnumbered). Note the almost flat articulation of the proximal phalanx to the metacarpal and the nearly vertical position of both elements. MC = metacarpal III, prox. PH = manual Phalanx III-1, dist. Ph = manual Phalanges III-2 through 4

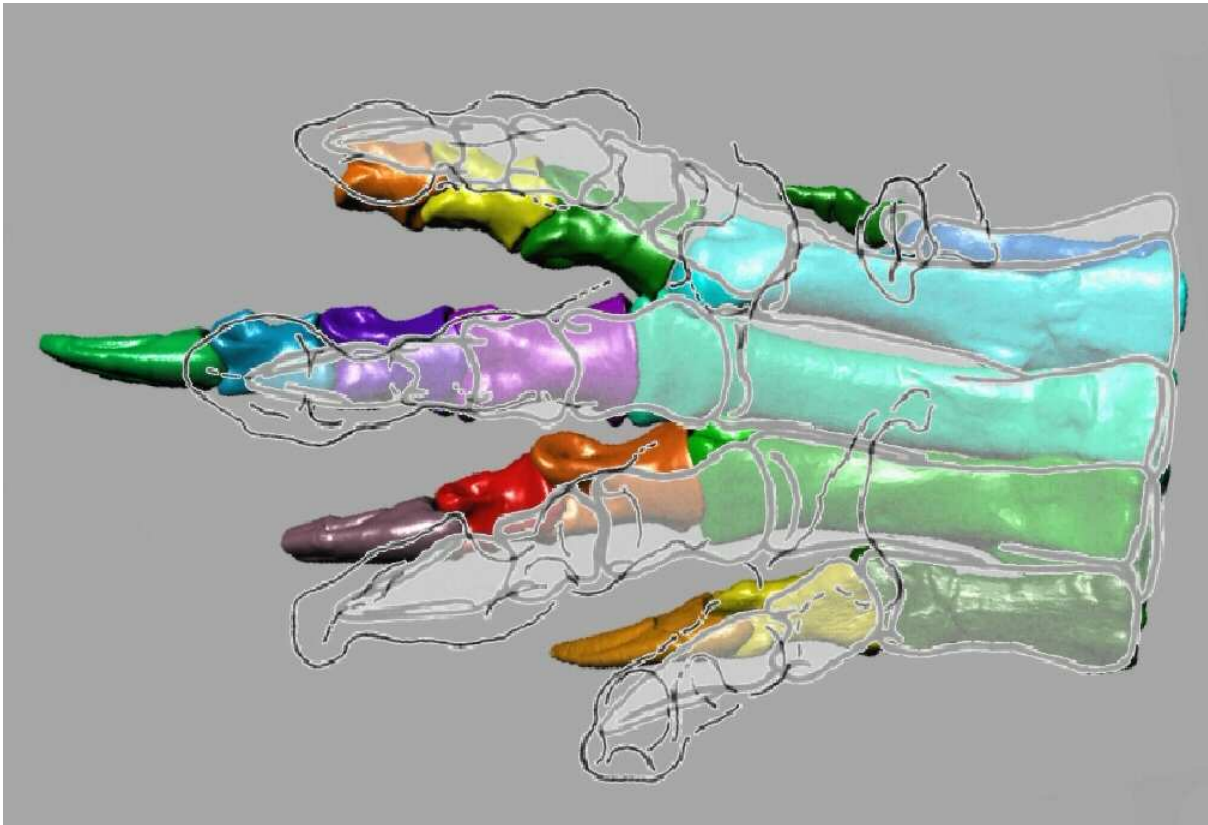


Figure 30: Sinistral pes of the virtual skeleton of GPIT 1 superimposed with fig. 10 (redrawn) from Porchetti and Nicosia (in press), which includes the outline drawing of the track of *Pseudotetrasauropus bipedoida* and the outline drawing of the sinistral pes of *Plateosaurus* from Galton (1985). Note the similar proportions of Galton's (1985) figure and the track, but significantly different proportions of GPIT 1.

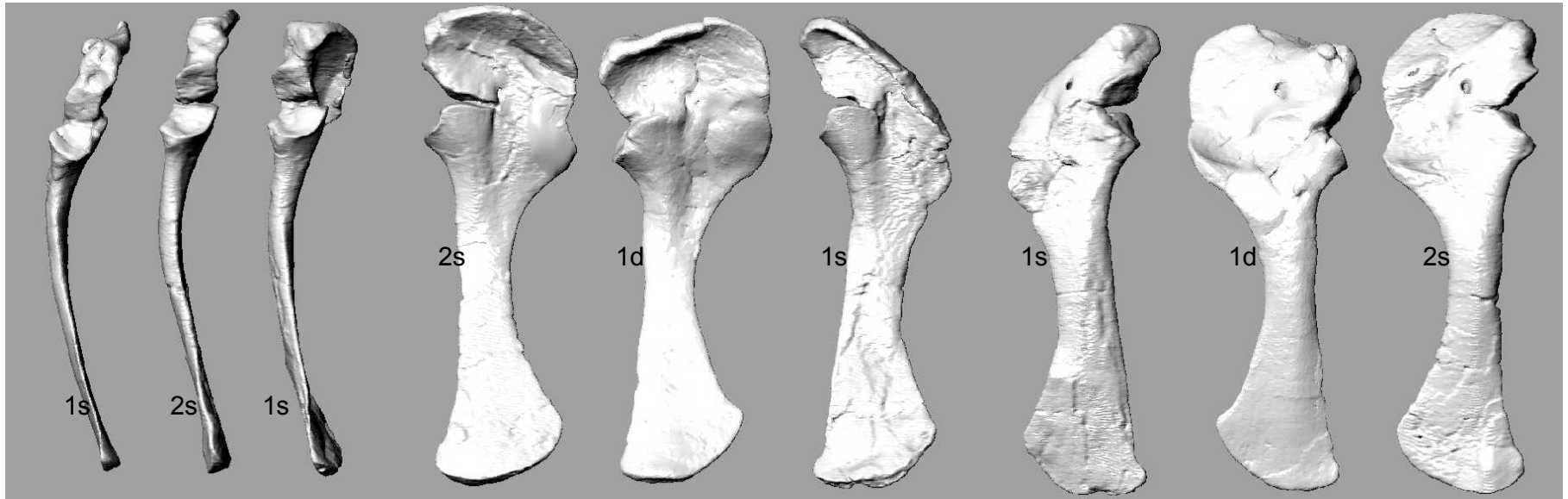


Figure 31: Comparison of the sinistral scapulacoracoid of GPIT 1 (1 s), the dextral scapulacoracoid of GPIT 1 (1 d) and the dextral scapulacoracoid of GPIT 2 (2 d) in ventral (left), medial (middle) and lateral (right) views. The sinistral scapulacoracoids have been mirrored.

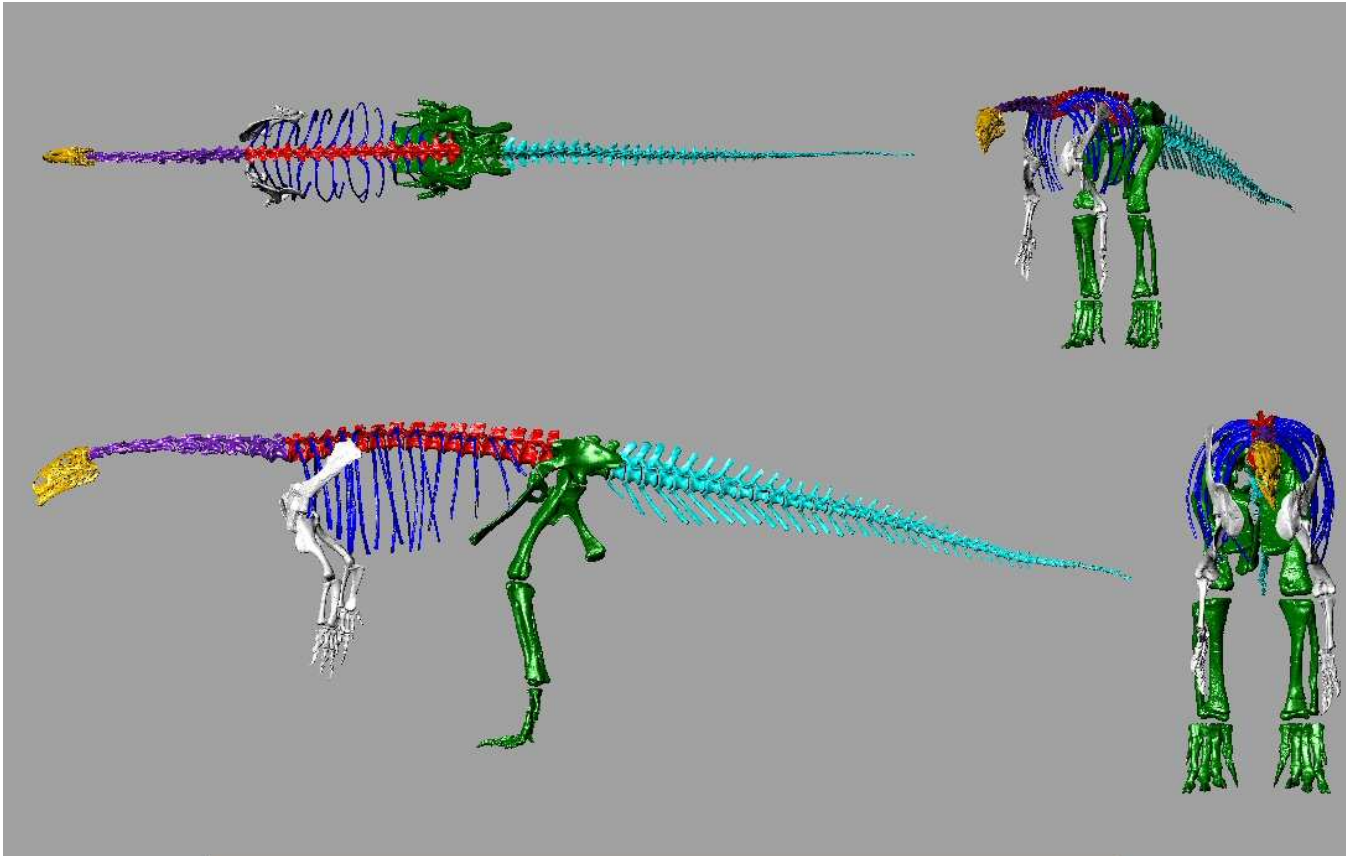


Figure 32: The virtual skeleton of *Plateosaurus engelhardti* (GPIT 1) in dorsal (top left), anterolateral (top right), lateral (bottom left) and frontal (bottom right) views.

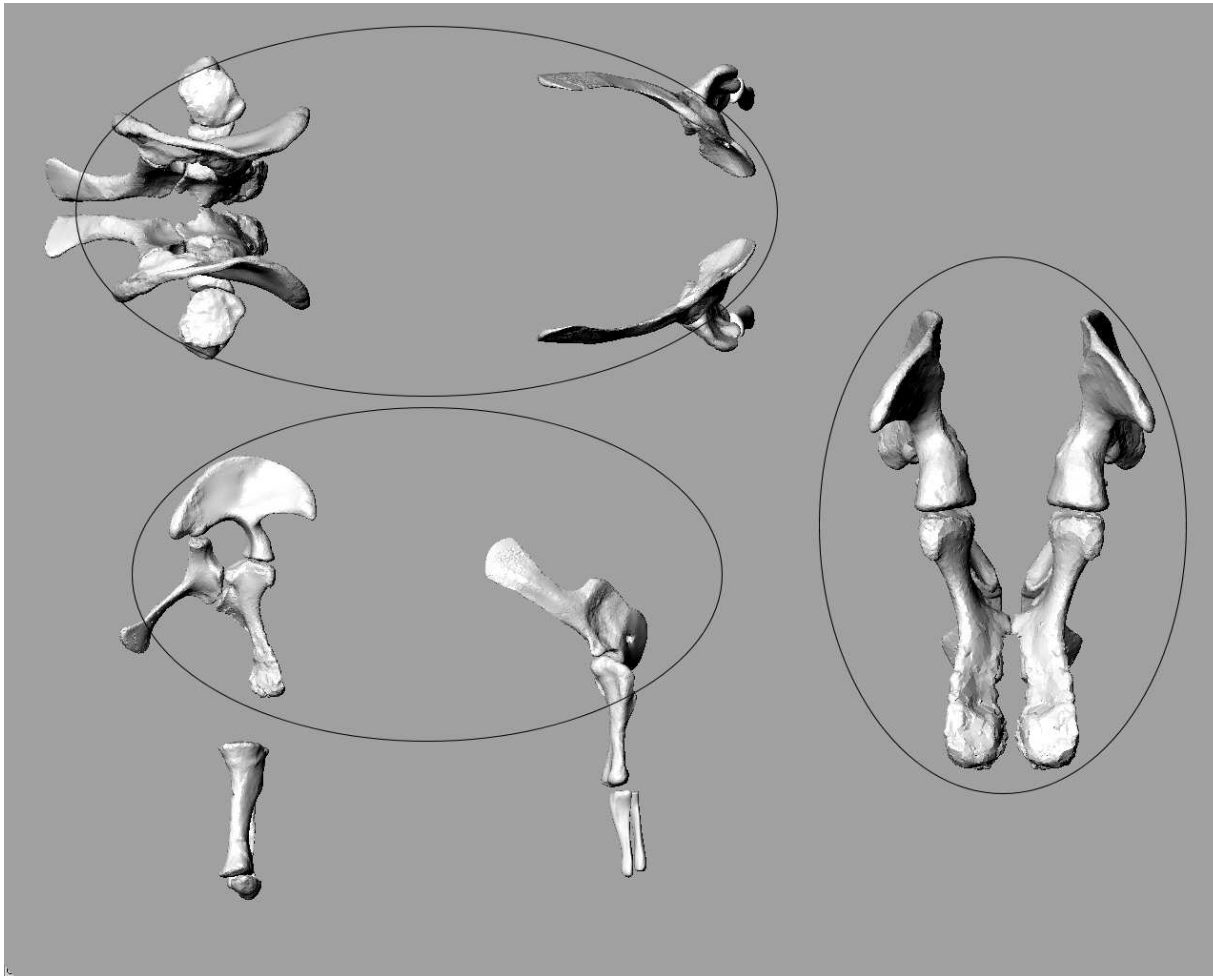


Figure 33: partial virtual skeleton of *Dicraeosaurus hansemanni* (MNHB exhibition mount) in dorsal (top left) and lateral (bottom left) views. Anterior view of the pelvic girdle on the right. Ellipses suggest a rough approximation of torso outline.

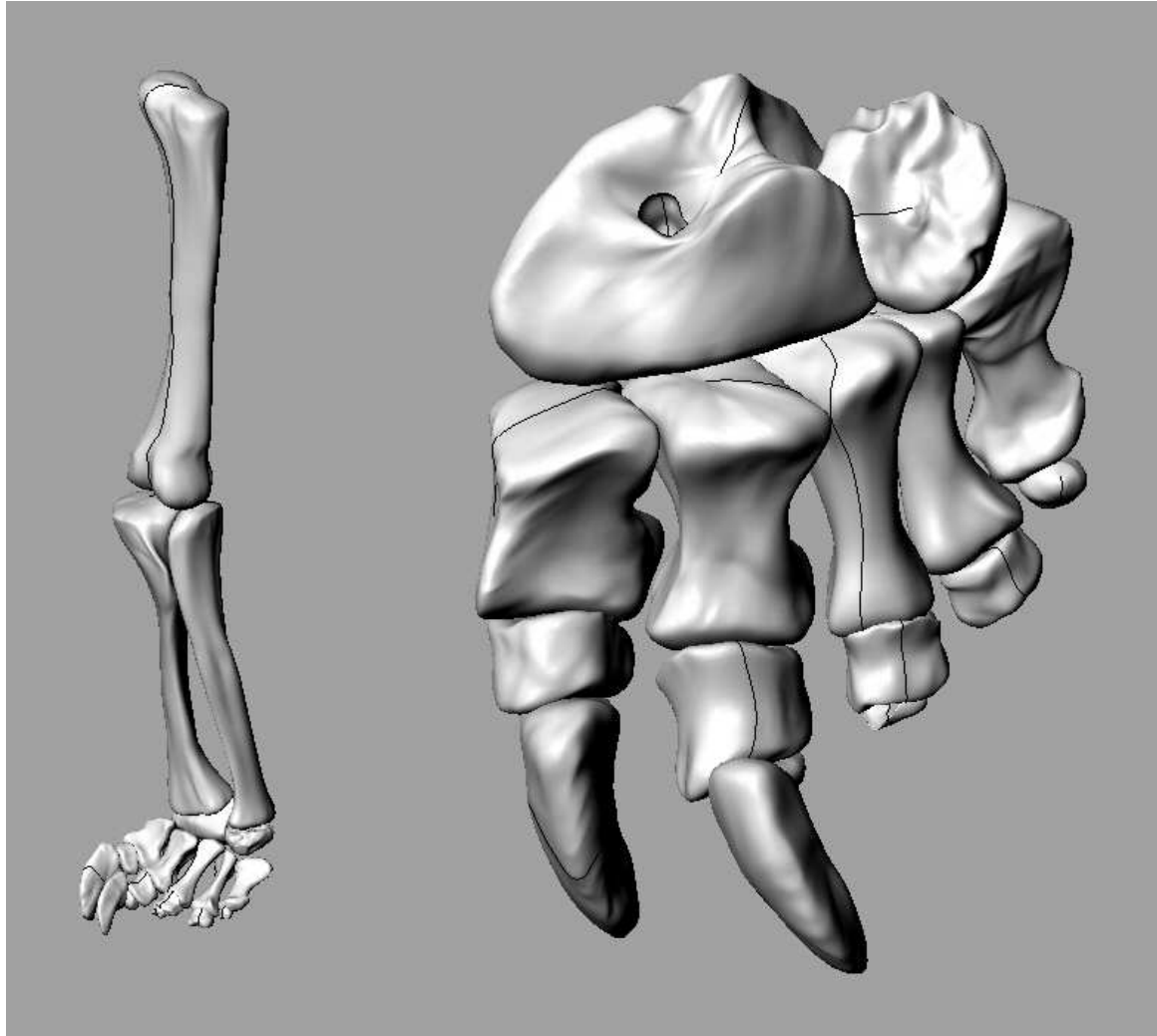


Figure 34: Sinistral hindlimb of *Barosaurus' africanus* (MNHB, MB.R.2662, MB.R.2576, MB.R.2616, MB.R.2563, MB.R.2370 [several]) from NURBS files. Right: dorsal view of the sinistral pes.

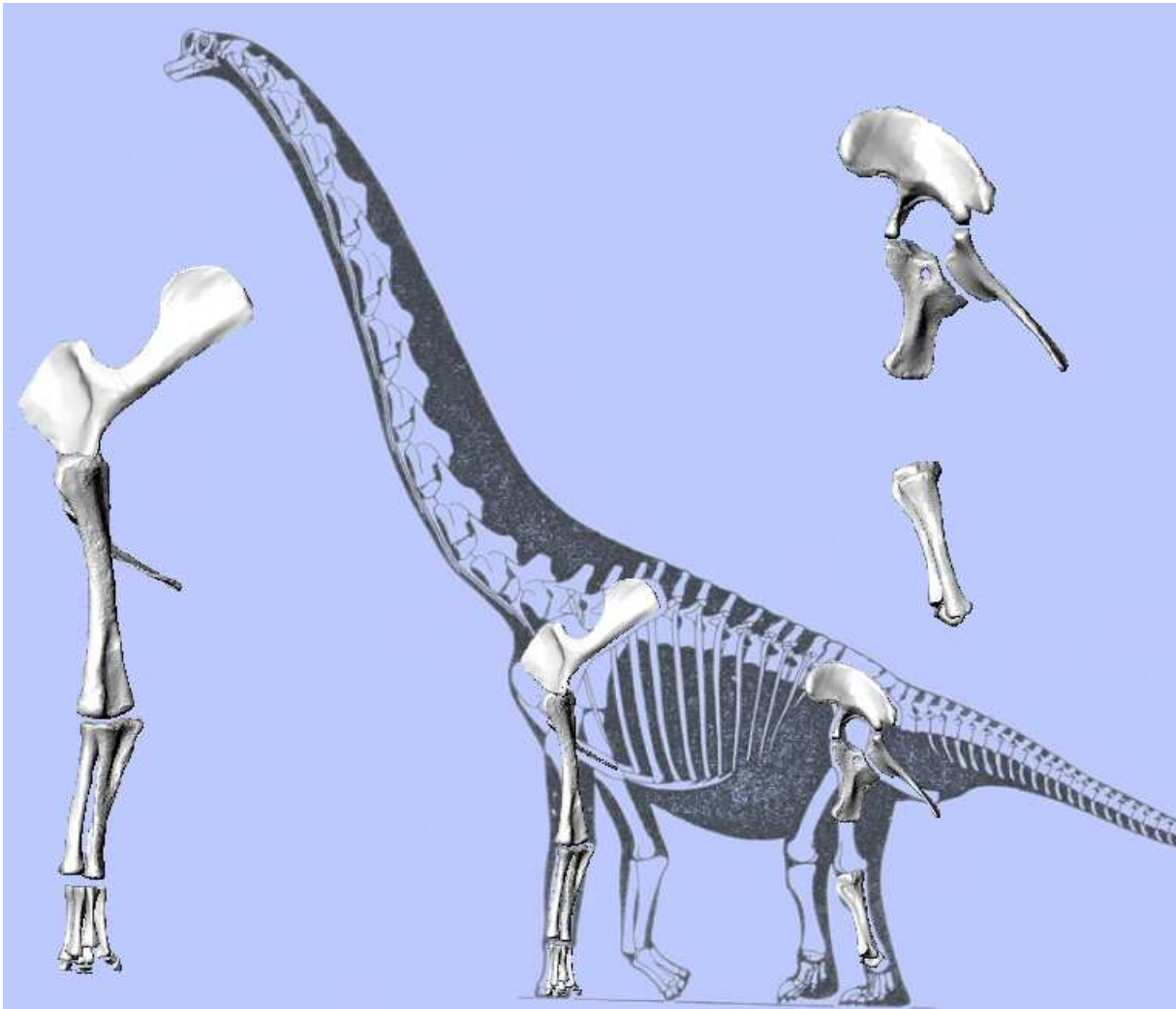


Figure 35: Sinistral forelimb (left), partial sinistral hindlimb (right) and both limbs of *Brachiosaurus brancai* arranged in front of the skeletal outline drawing by Paul (2003). Material from MNHB.

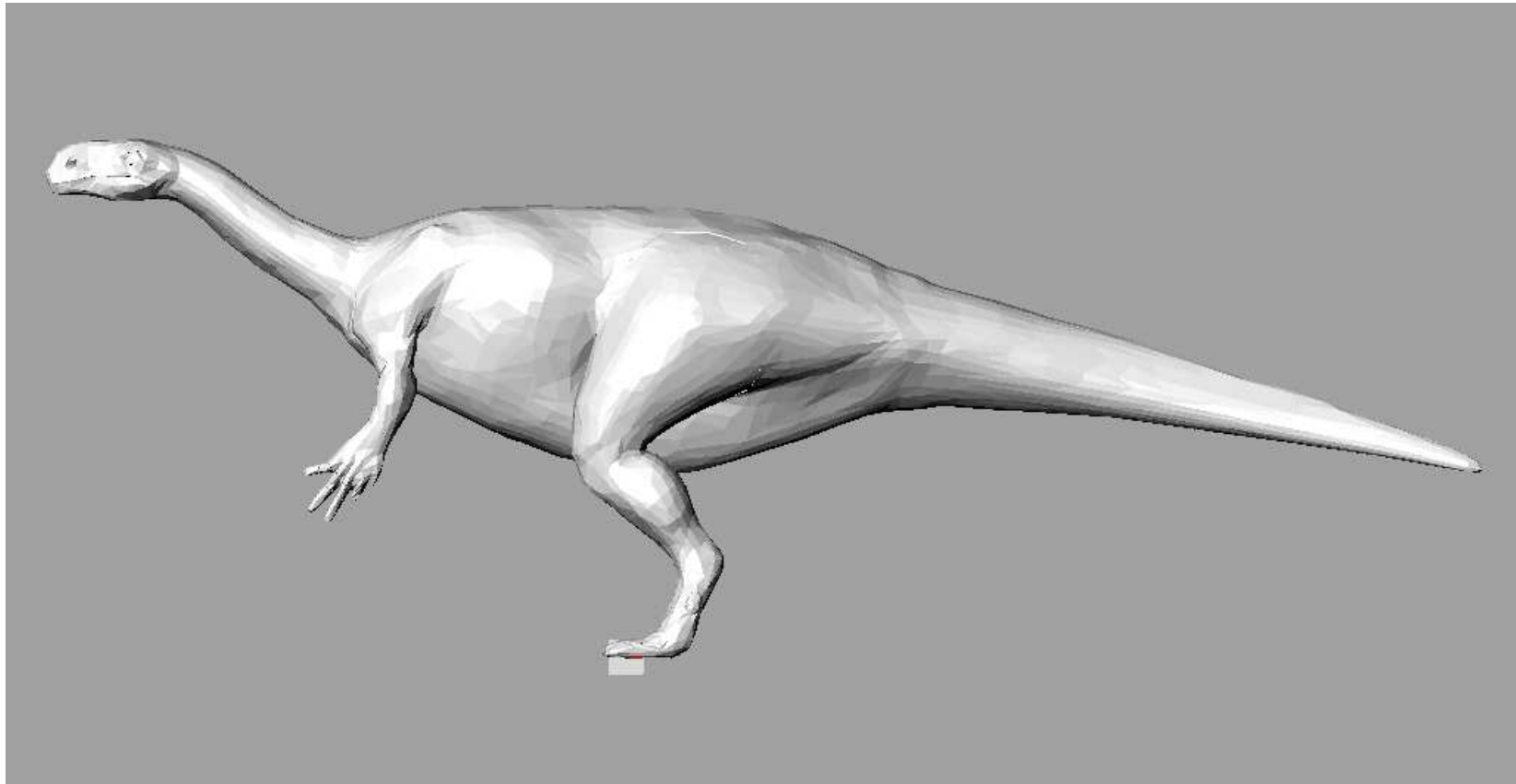


Figure 36: 3D model based on the laser scan of GPIT 1, first version. Note the overly long thigh.

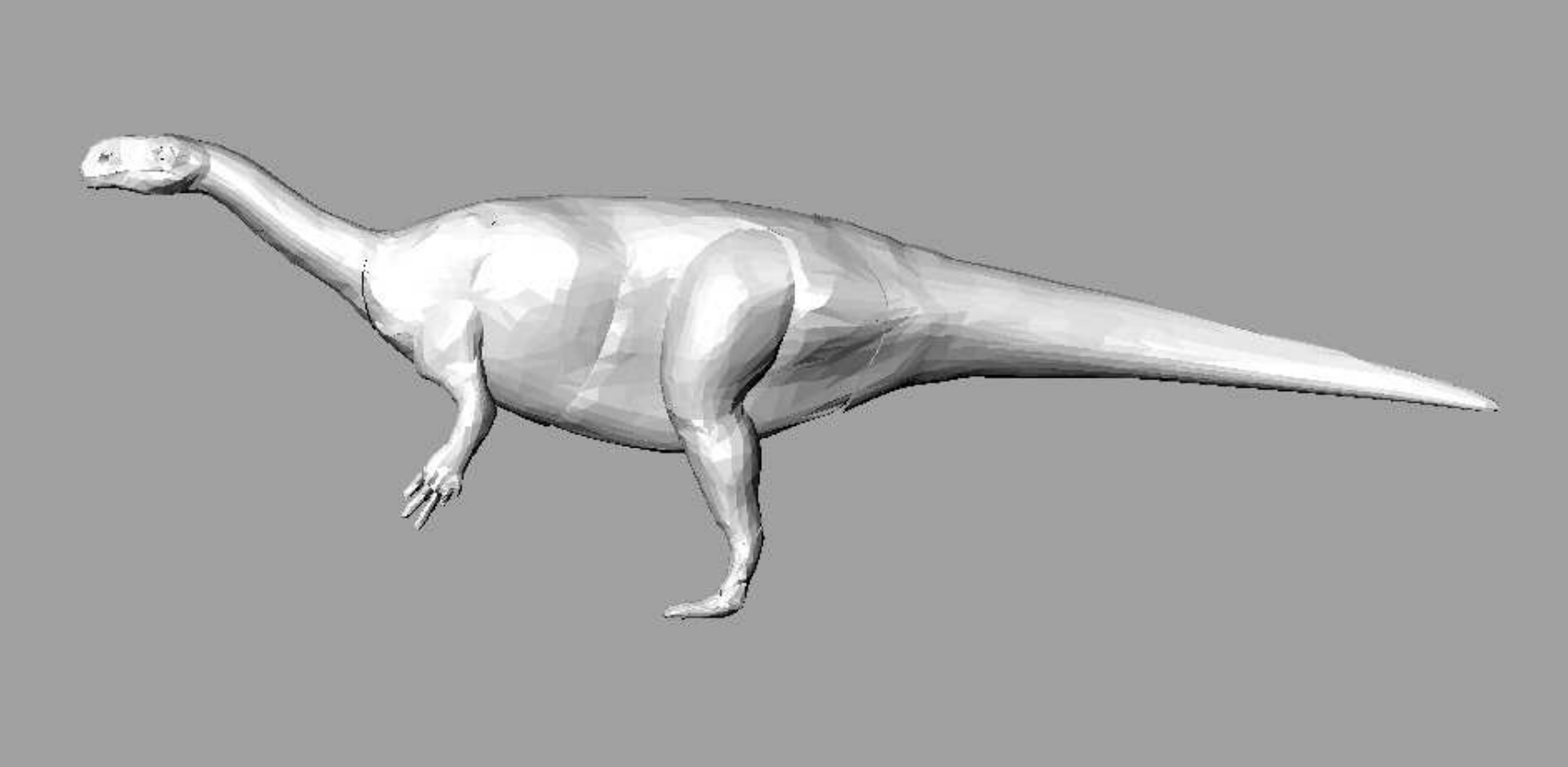


Figure 37: Corrected 3D model based on the laser scan of GPIT. Note the relatively large torso and strongly muscled limbs.

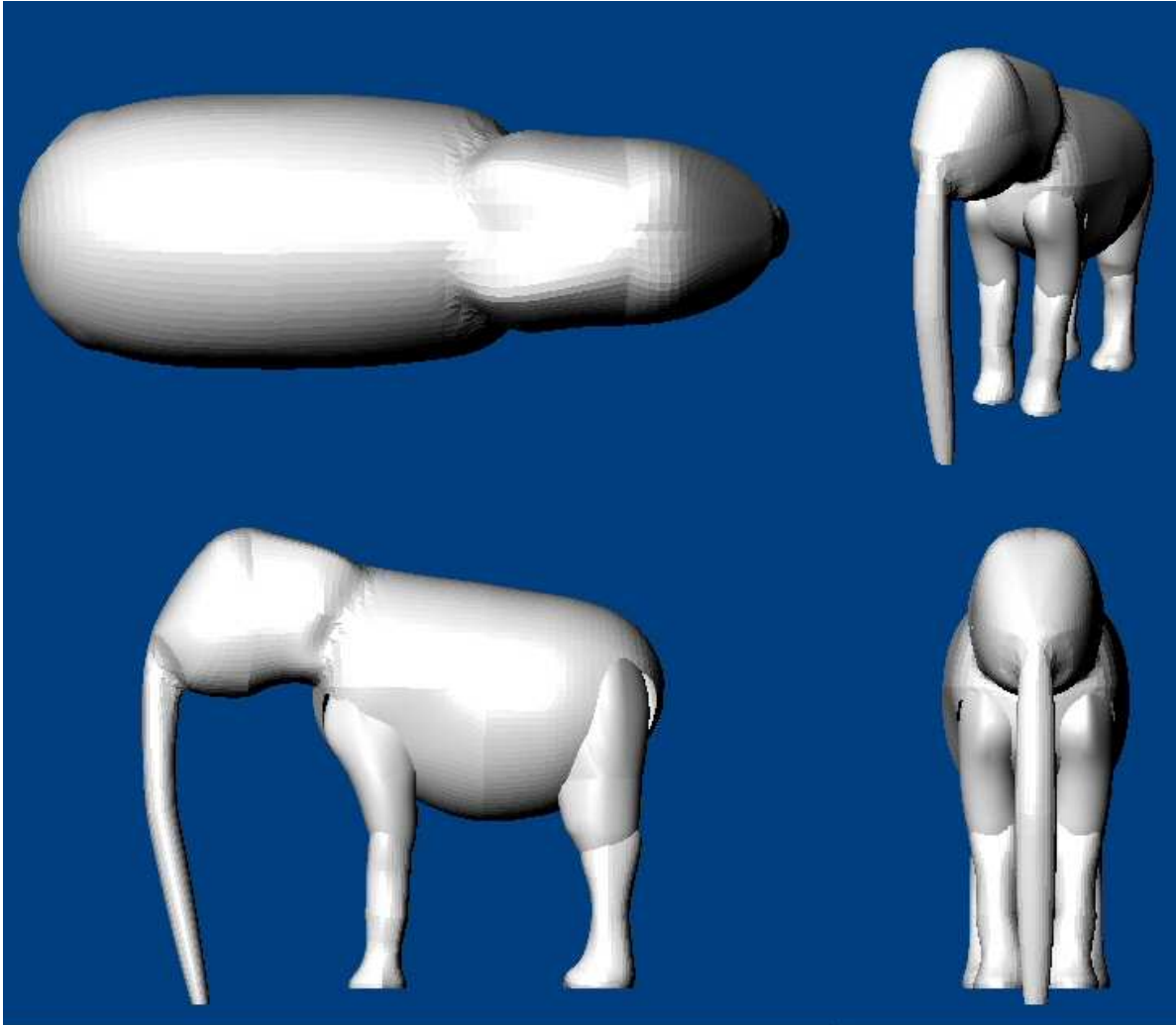


Figure 38: 3D model of *Elephas maximus* based on laser scan in dorsal (top left), oblique (top right), lateral (bottom left) and anterior (bottom right) views. Note that the ears have been omitted because of their small mass.

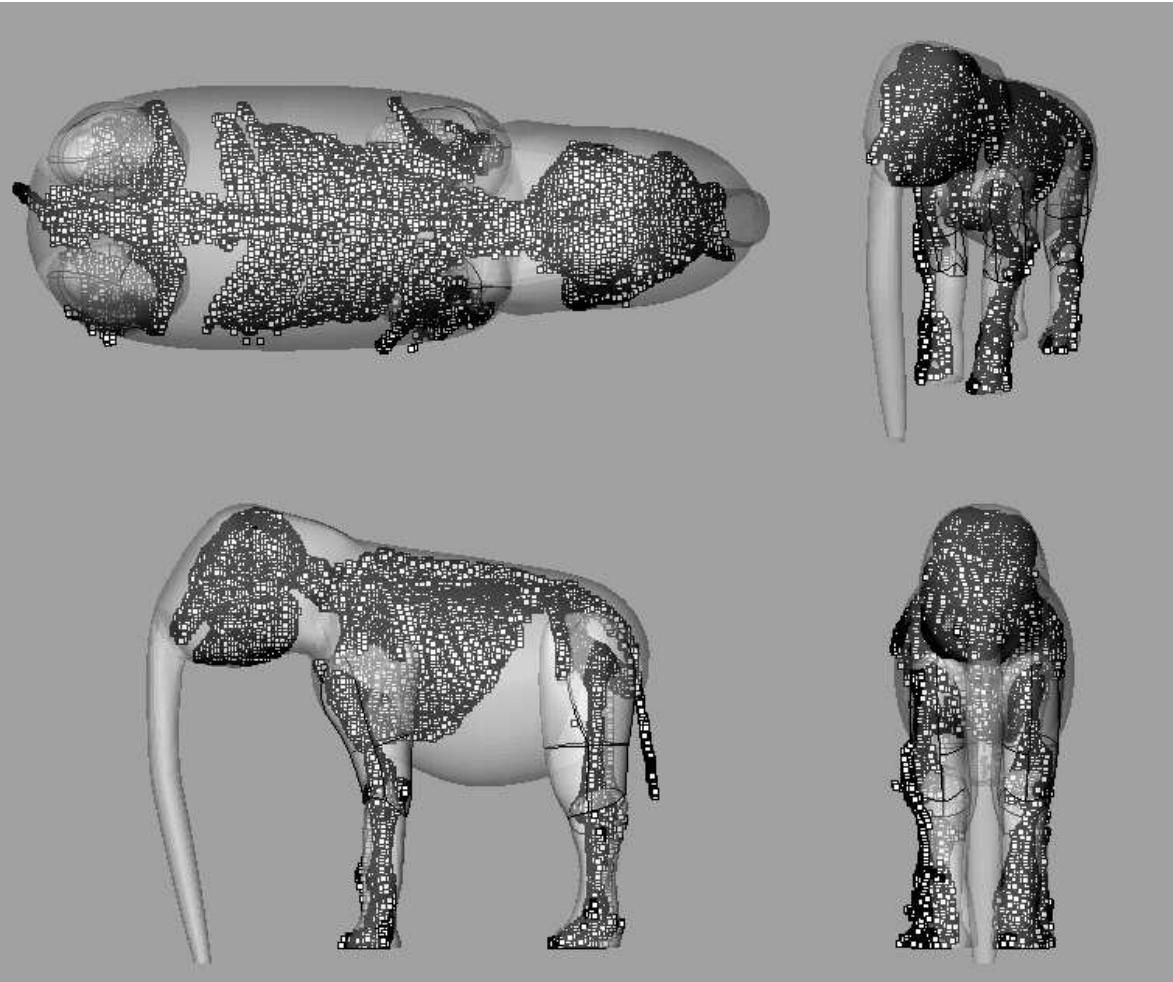


Figure 39: 3D model of *Elephas maximus* in identical aspects as in Figure 38 in 'ghosted' view, showing the underlying point cloud file of the laser scan.

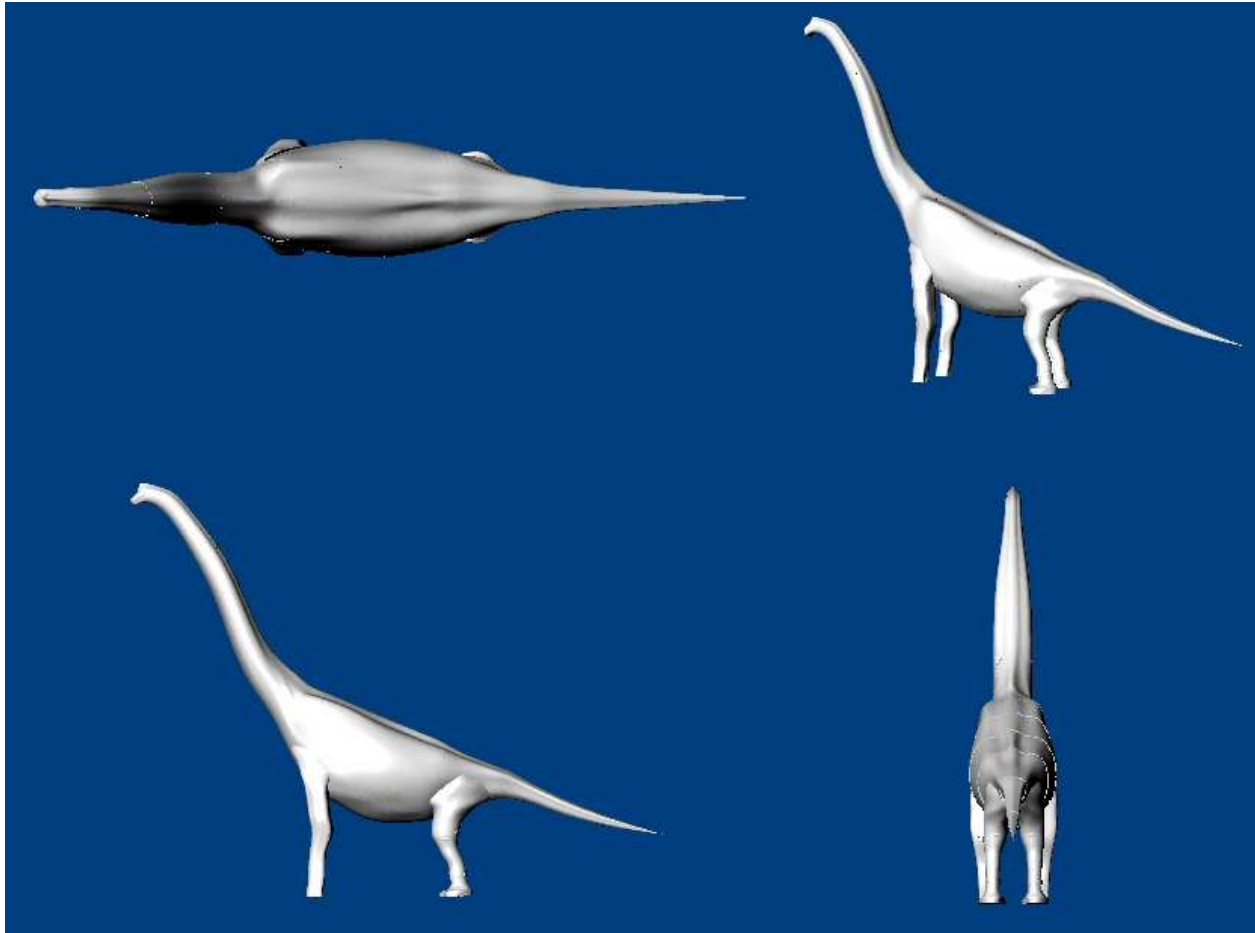


Figure 40: 3D model of *Brachiosaurus brancai* based on skeletal drawings from Paul (2003) in dorsal (top left), oblique (top right), lateral (bottom left) and posterior (bottom right) views.

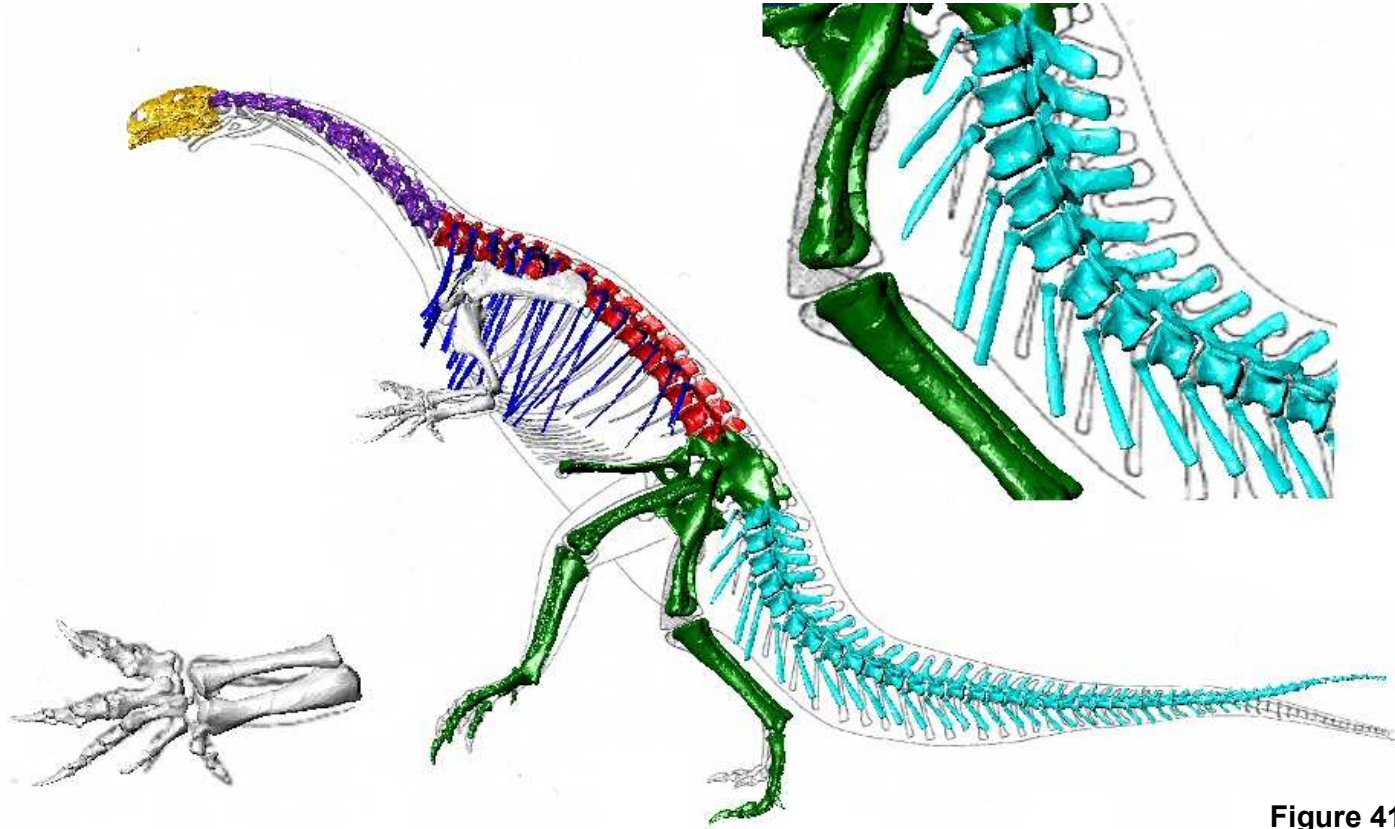


Figure 41: Virtual skeleton posed to conform to the reconstruction by Huene (1926). Inset on right shows detail of the massive divergence from the neutral position required in the anterior tail, inset on left shows disarticulated manus.

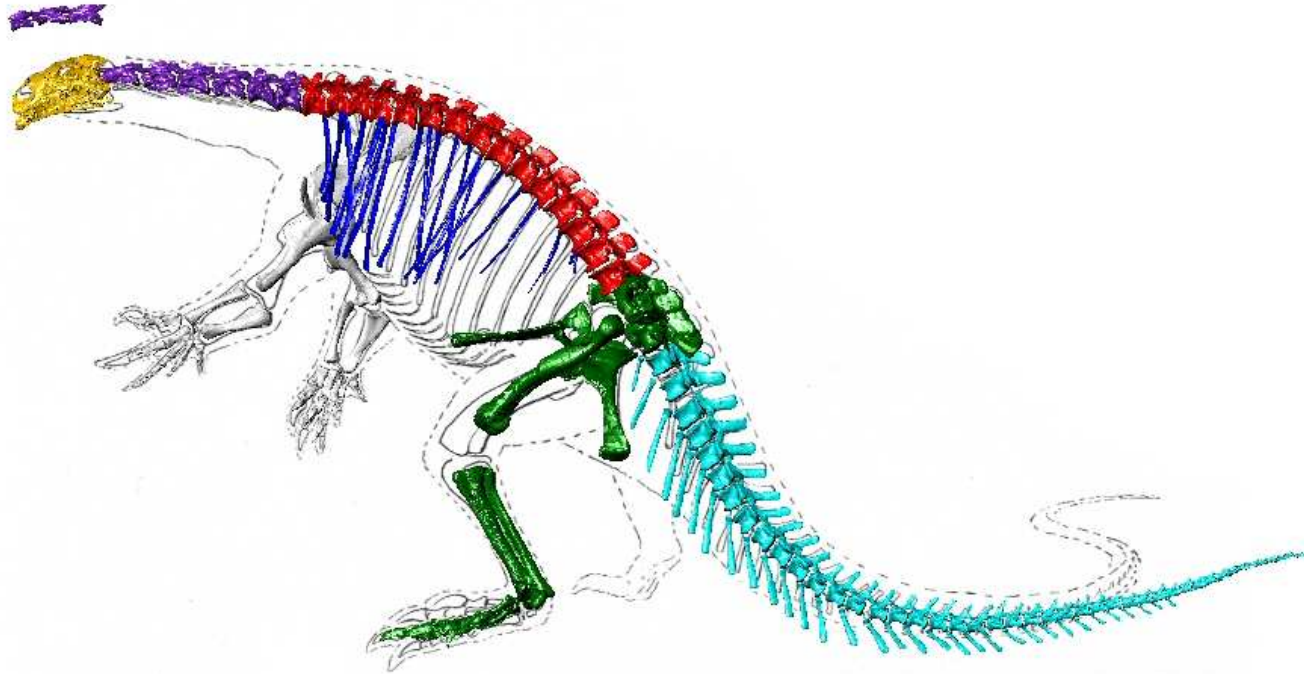


Figure 42: Virtual skeleton posed to conform to the reconstruction by Jaekel (1913-14). Note the different neck length, the disarticulated radius and ulna and the large gap between femur and tibia

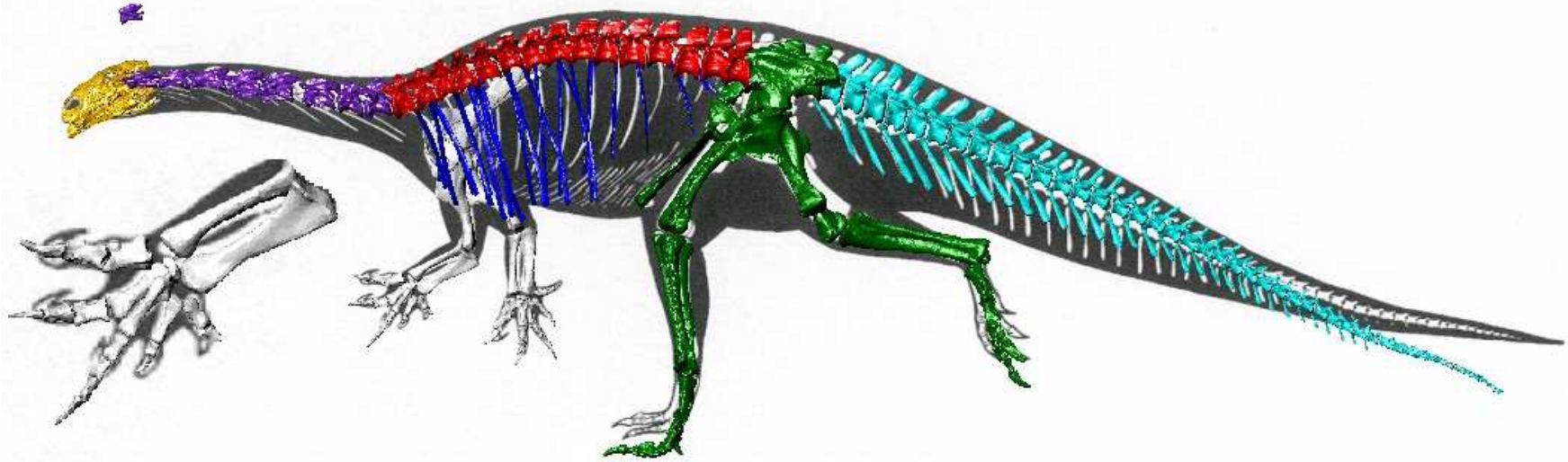


Figure 43: Virtual skeleton posed to conform to the outlined skeletal drawing by Weishampel and Westphal (1986). Note the scaling problems with the cervical vertebrae and the hind limbs. Inset shows closer view of the disarticulated manus. Note that the ulna and radius are correctly articulated.

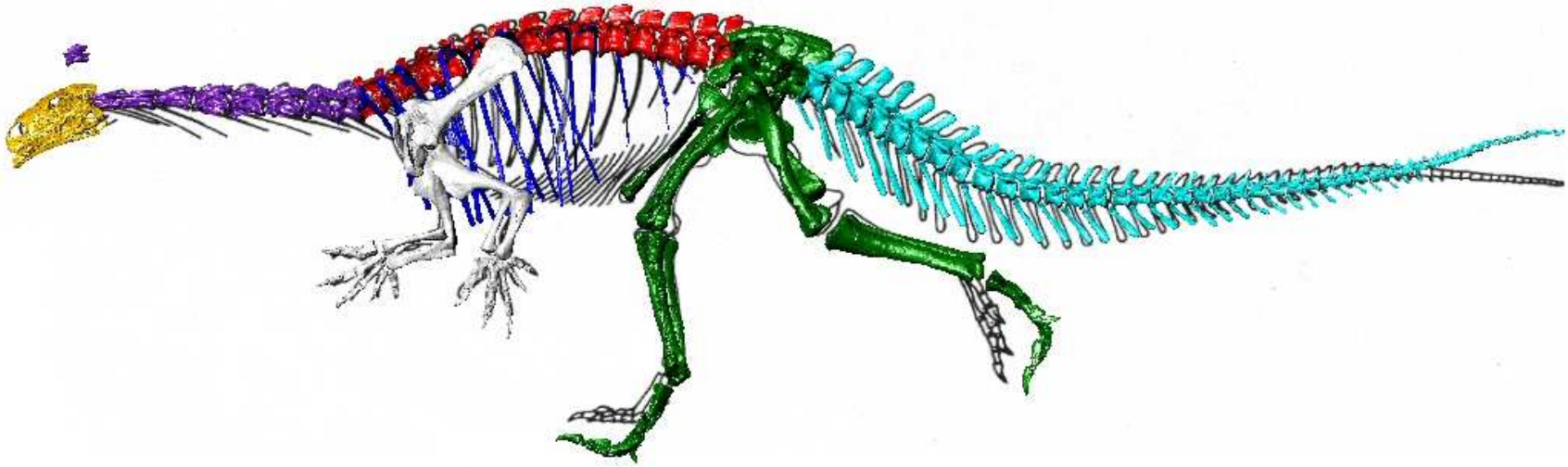


Figure 44: Virtual skeleton posed to conform to the reconstruction drawing by Galton (1990). Note the disarticulated manus and scaling issues in the neck and limbs. The scapulae are positioned very high on the ribcage.

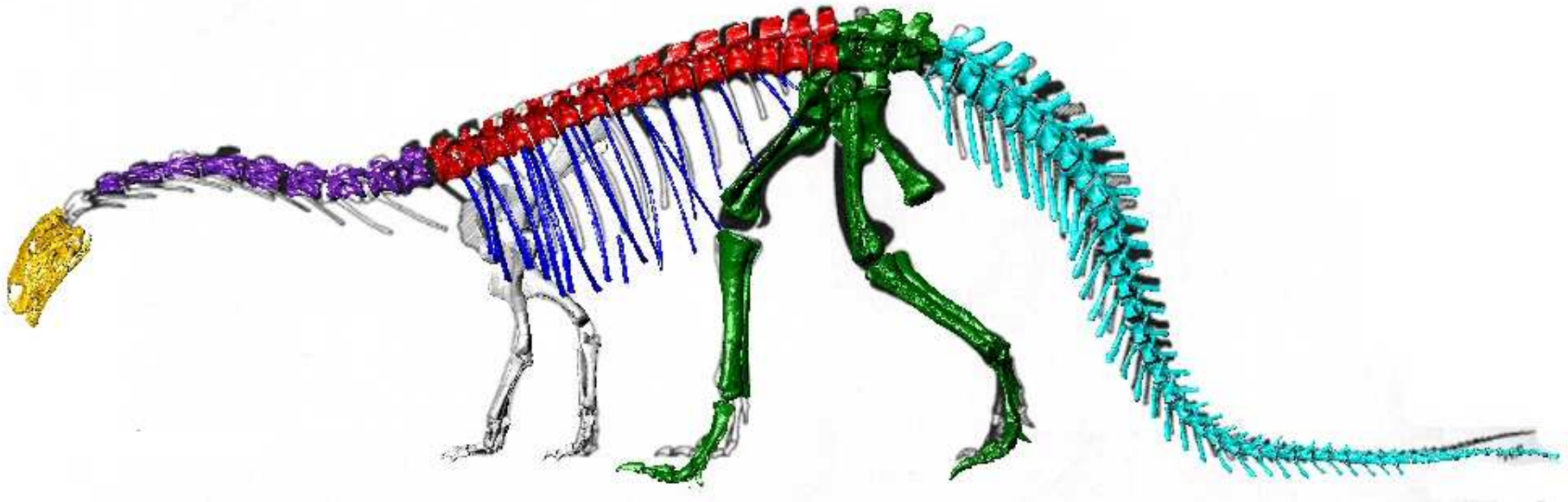


Figure 45: Virtual skeleton posed to conform to the skeletal drawing of Wellnhofer (1994). Note the difference in neck length, the forced quadrupedal position including the length discrepancy in the hind limbs and the forcibly bent tail.

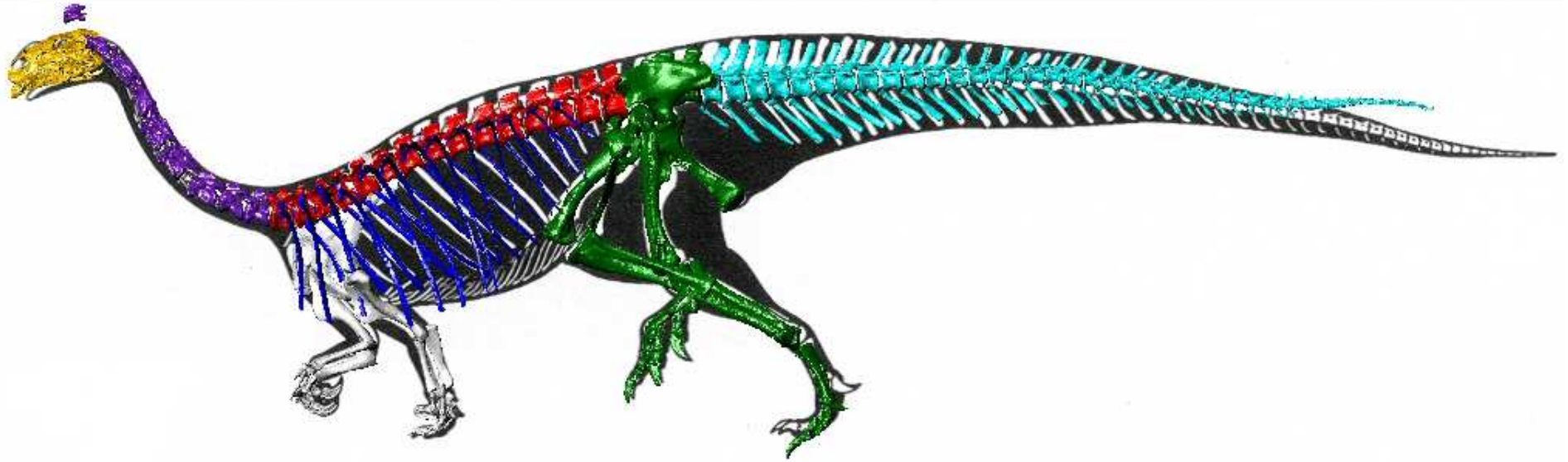


Figure 46: Virtual skeleton posed to conform to the outlined skeletal drawing of Paul (1987). Note the different neck length, the impossible articulation of the right ankle and the problems associated with the forced quadrupedal posture.

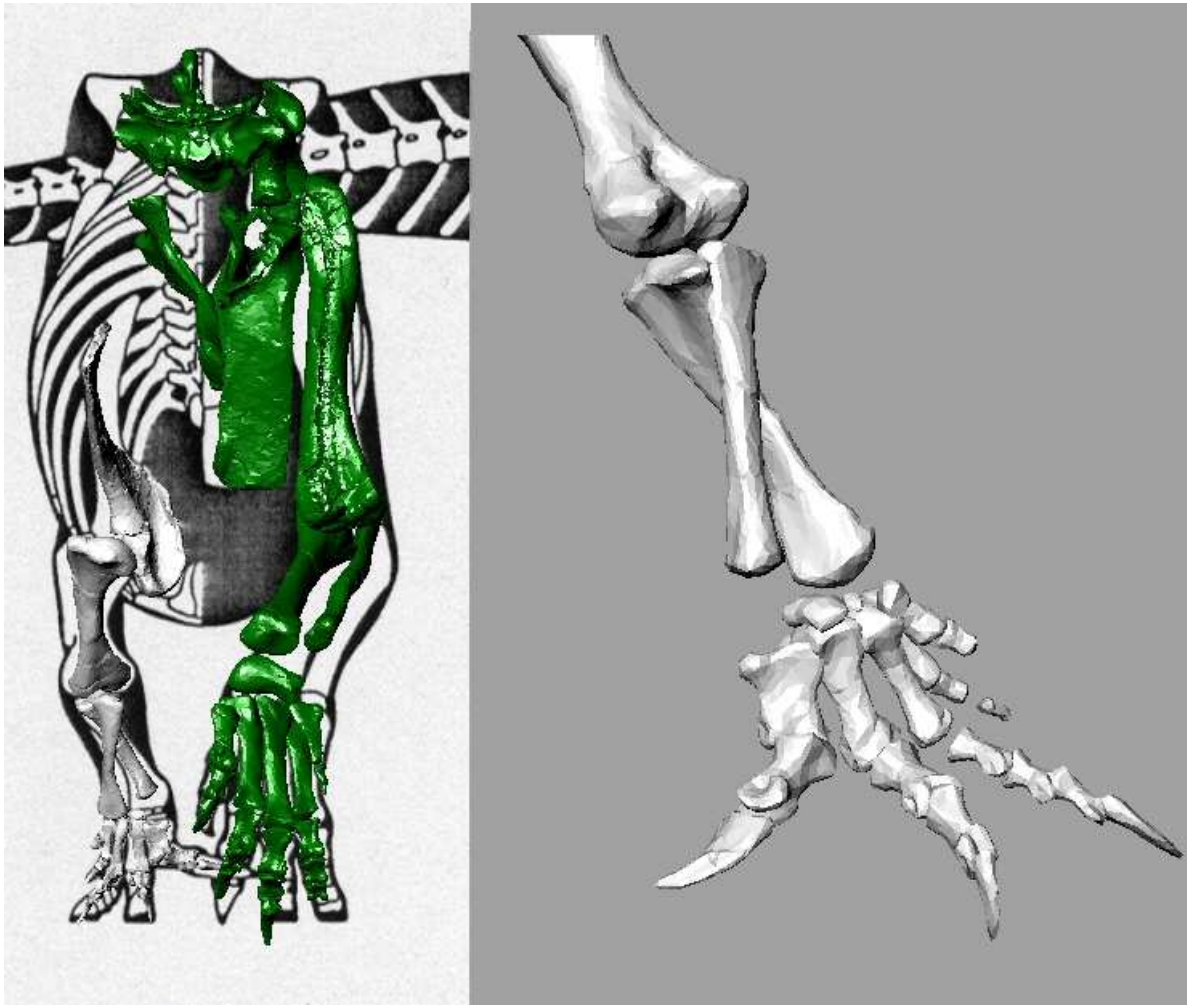


Figure 47: Left: Virtual skeleton posed to conform to the outlined skeletal drawing in anterior view of Paul (1987). Note the disarticulated ankle and the collision of tibia, fibula and femur. Right: Closer view of the left lower arm. Note how the radius intersects the ulna. Digit 1 is disarticulated from metacarpal 1.

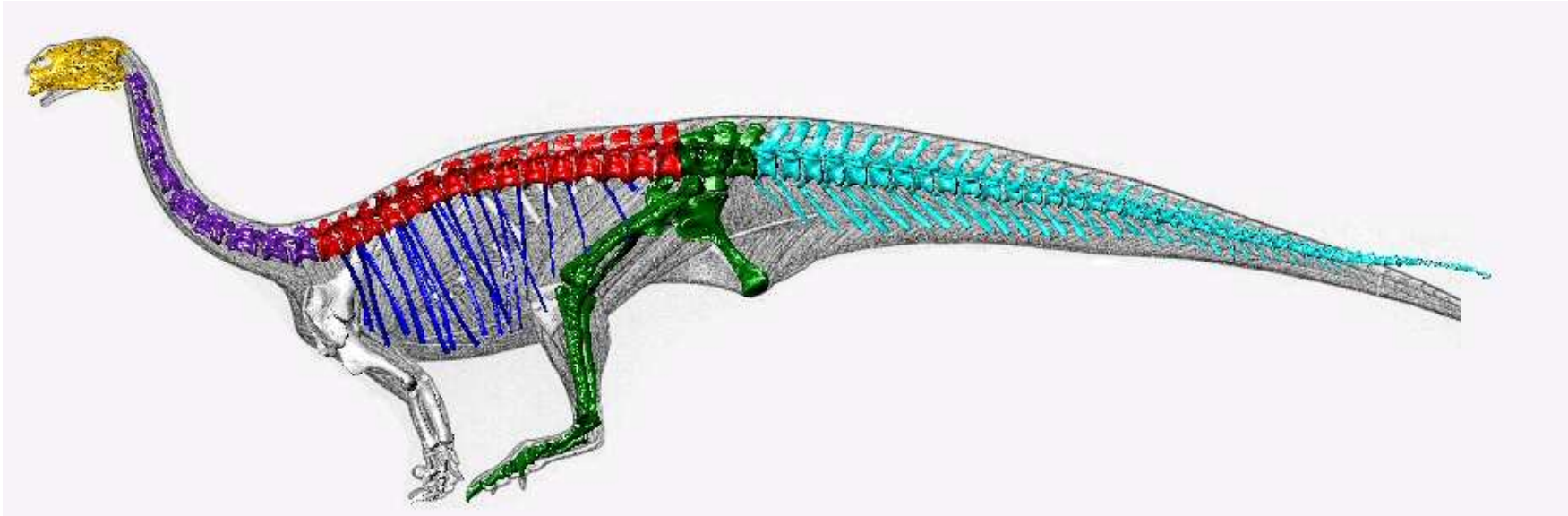


Figure 48: Virtual skeleton posed to conform to the musculoskeletal reconstruction drawing by Paul (1987). Note the length difference in the femur.

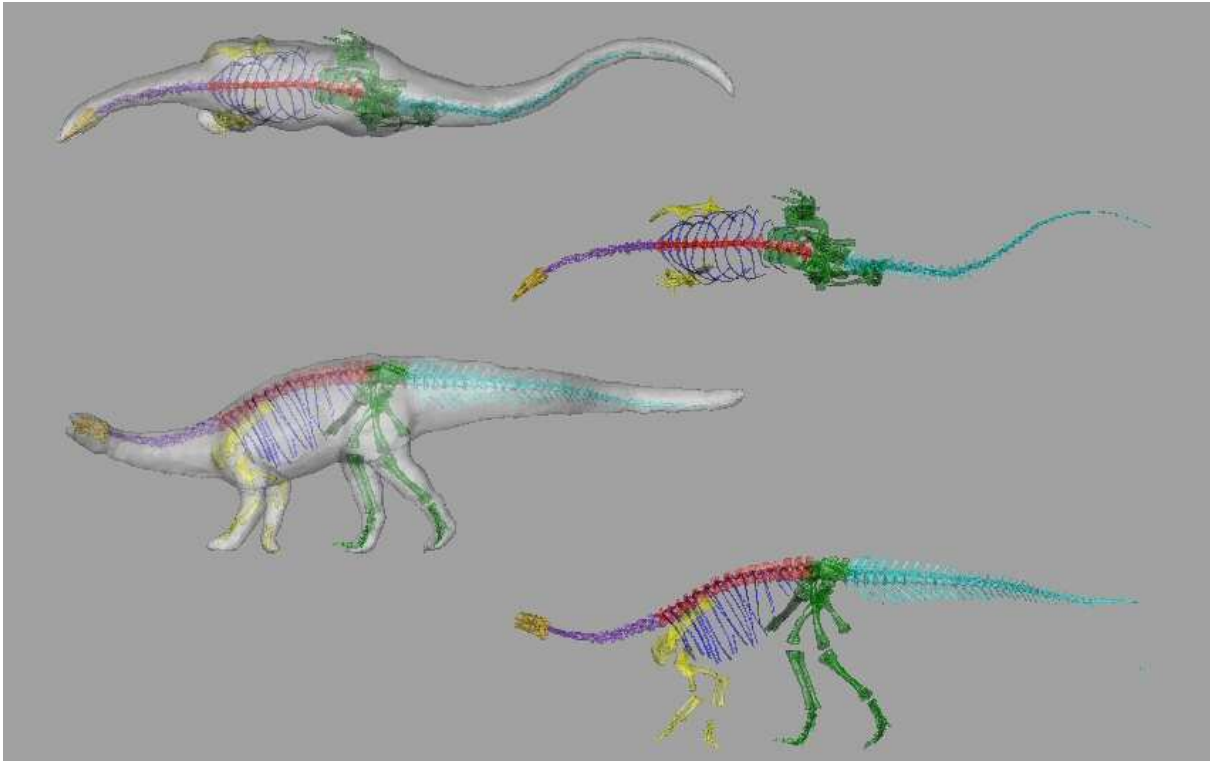


Figure 49: Virtual skeleton posed to conform to the Bullyland® toy model created in cooperation with the SMNS. Left top and bottom show dorsal and lateral views with the toy model in 'ghosted' view, right top and bottom show same views with the toy model hidden.

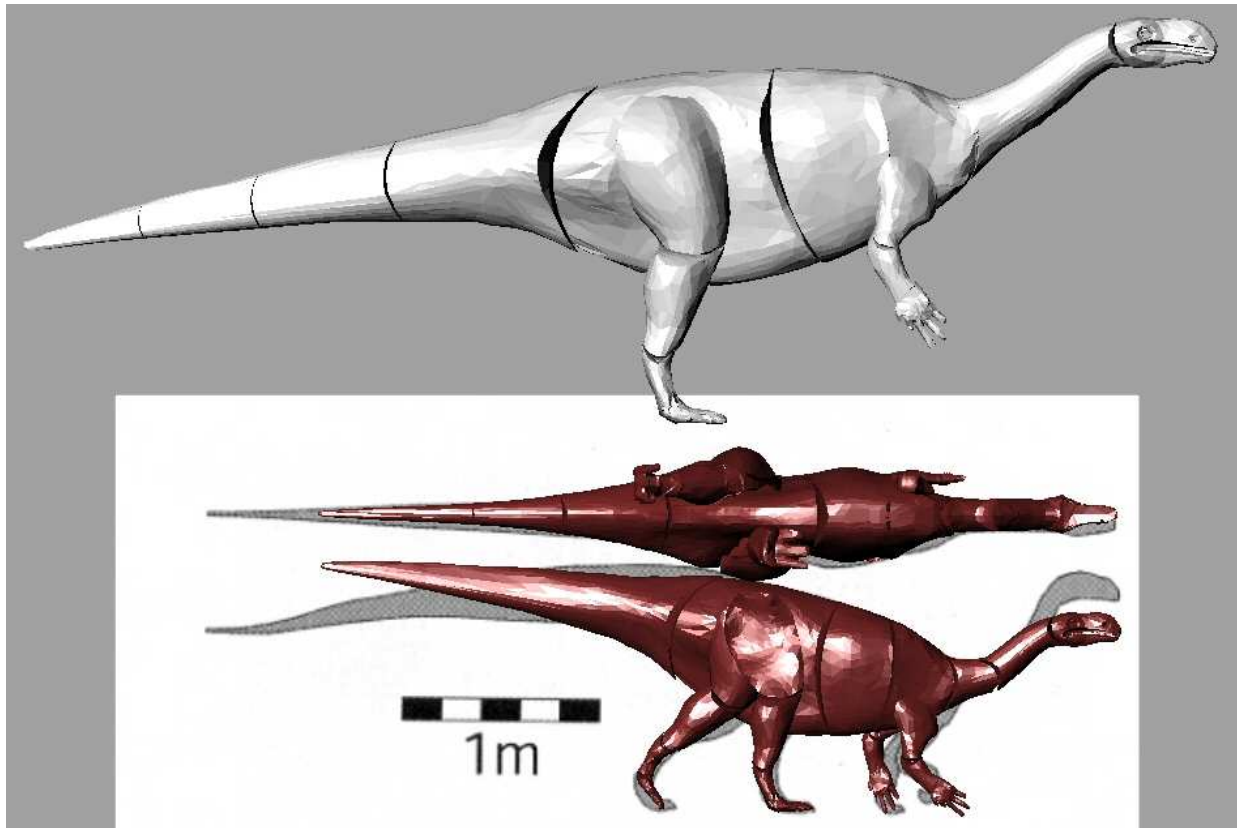


Figure 50: 3D model of *Plateosaurus* posed to conform to the drawing from Henderson (2007), scaled according to the scale bar (dark red). On top: model scaled to size of GPIT 1.

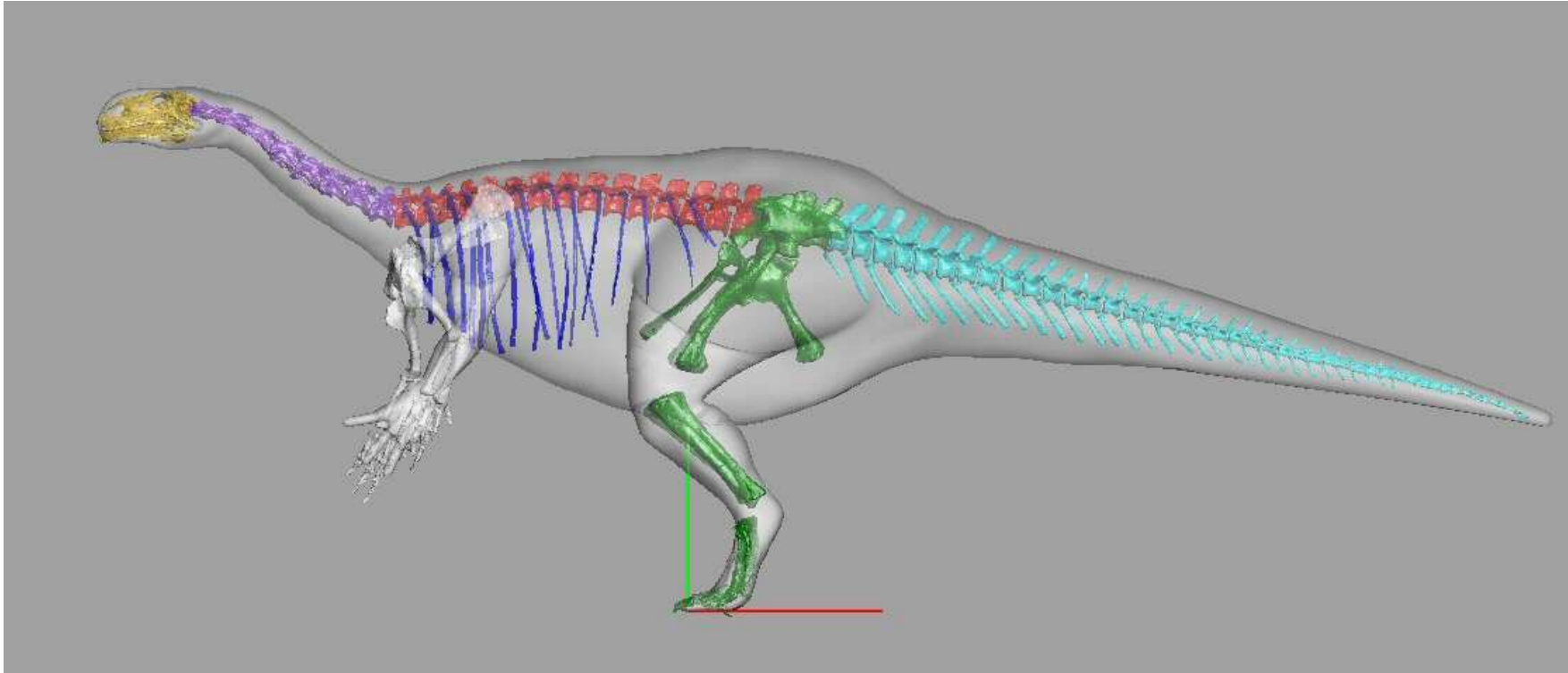


Figure 51: Virtual skeleton and own 3D model in comparison. Note the scaling problems on the torso, upper arm and in the hindlimb. Also note the excess muscle mass on the pelvic region.

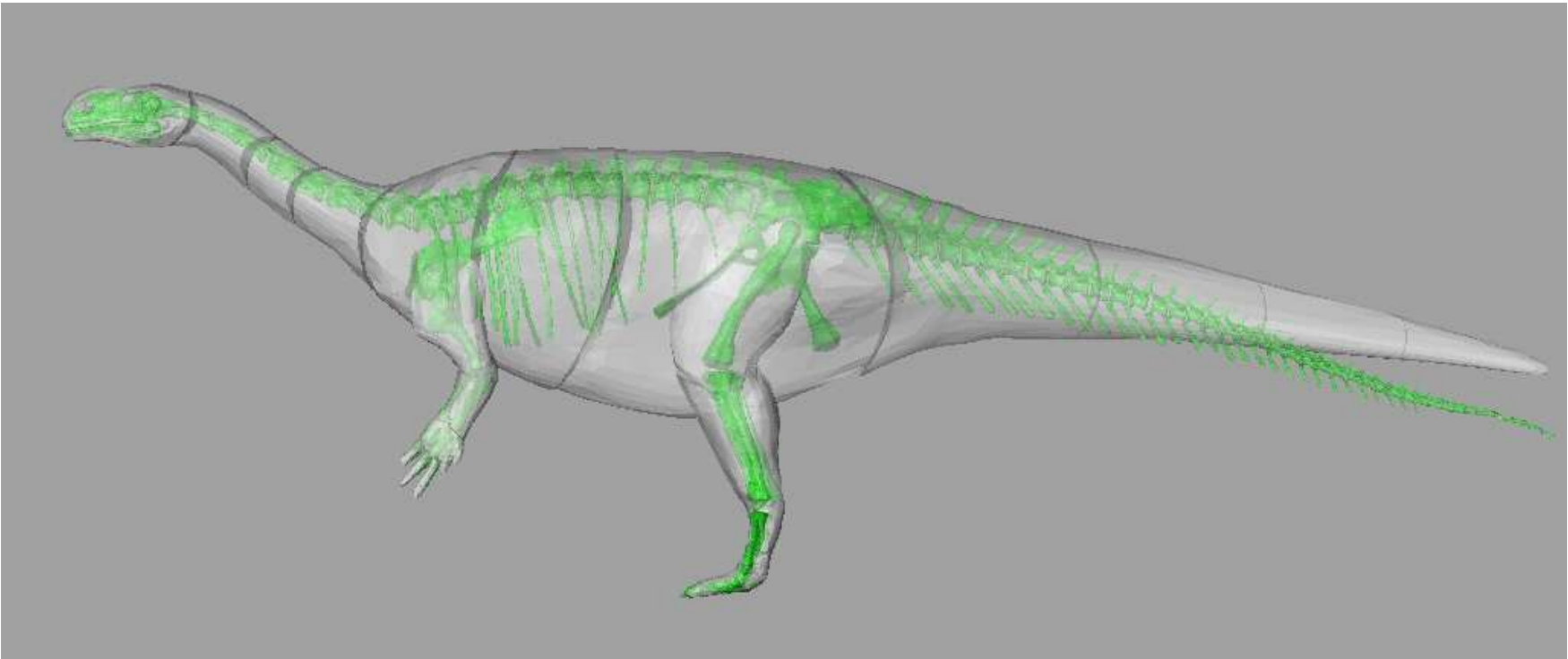


Figure 52: Virtual skeleton and corrected own 3D model compared in ghosted view.

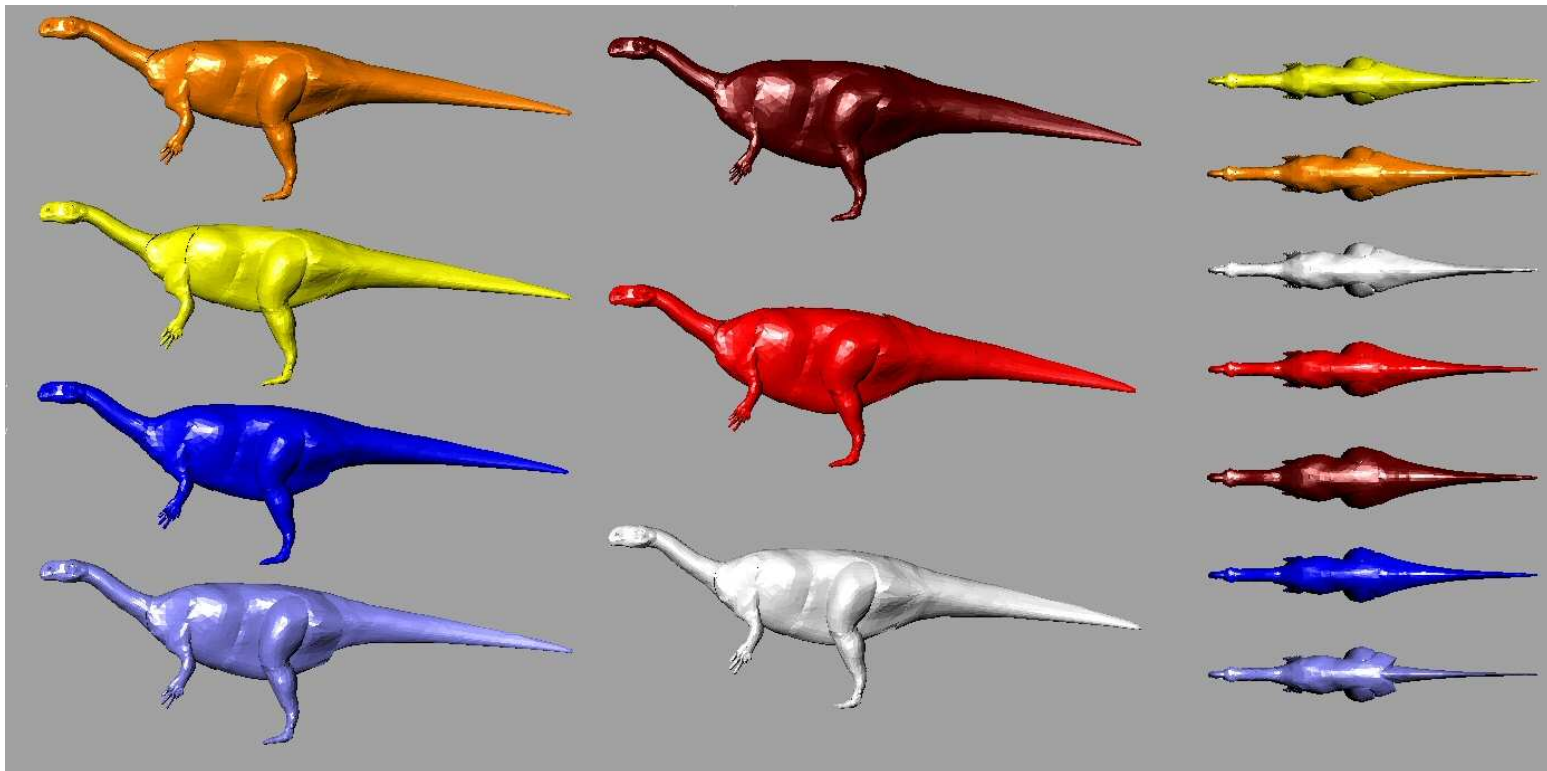


Figure 53: Versions of the 3D model with varying amounts of soft tissue. Left: lateral view. Right: dorsal view. Grey = normal, red = fattened 1D, dark red = fattened 2D, orange = slimmer 1 D, yellow = slimmer 2D, dark blue = tail slimmer 1 D, light blue = tail slimmer 2 D.



Figure 54: Screenshot from a video file taken at the Tierpark Berlin of a walking African elephant (*Loxodonta africana*). The animal was moving at a steady walk. Note the blurring of both the left manus and pes, which proves that they both are being protracted at the same time.

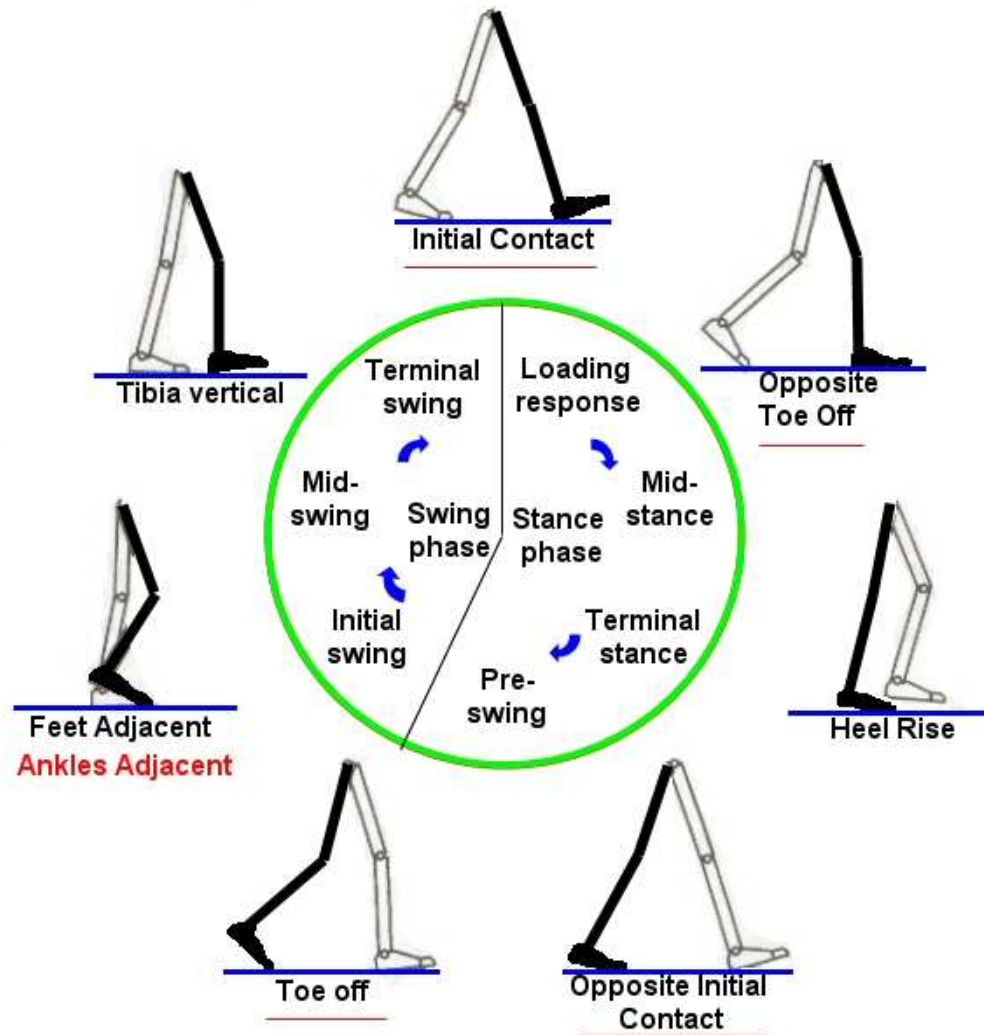


Figure 55: Scheme of a walking cycle of human locomotion after Whittle (1996). Distinct positions useful for dinosaur locomotion modeling are underlined in red. 'Ankles adjacent' replaces 'Feet adjacent'. Redrawn and edited after Whittle (1996).

Mallison, H.: Virtual Dinosaurs - CAD and CAE Modeling Methods for Vertebrate Paleontology

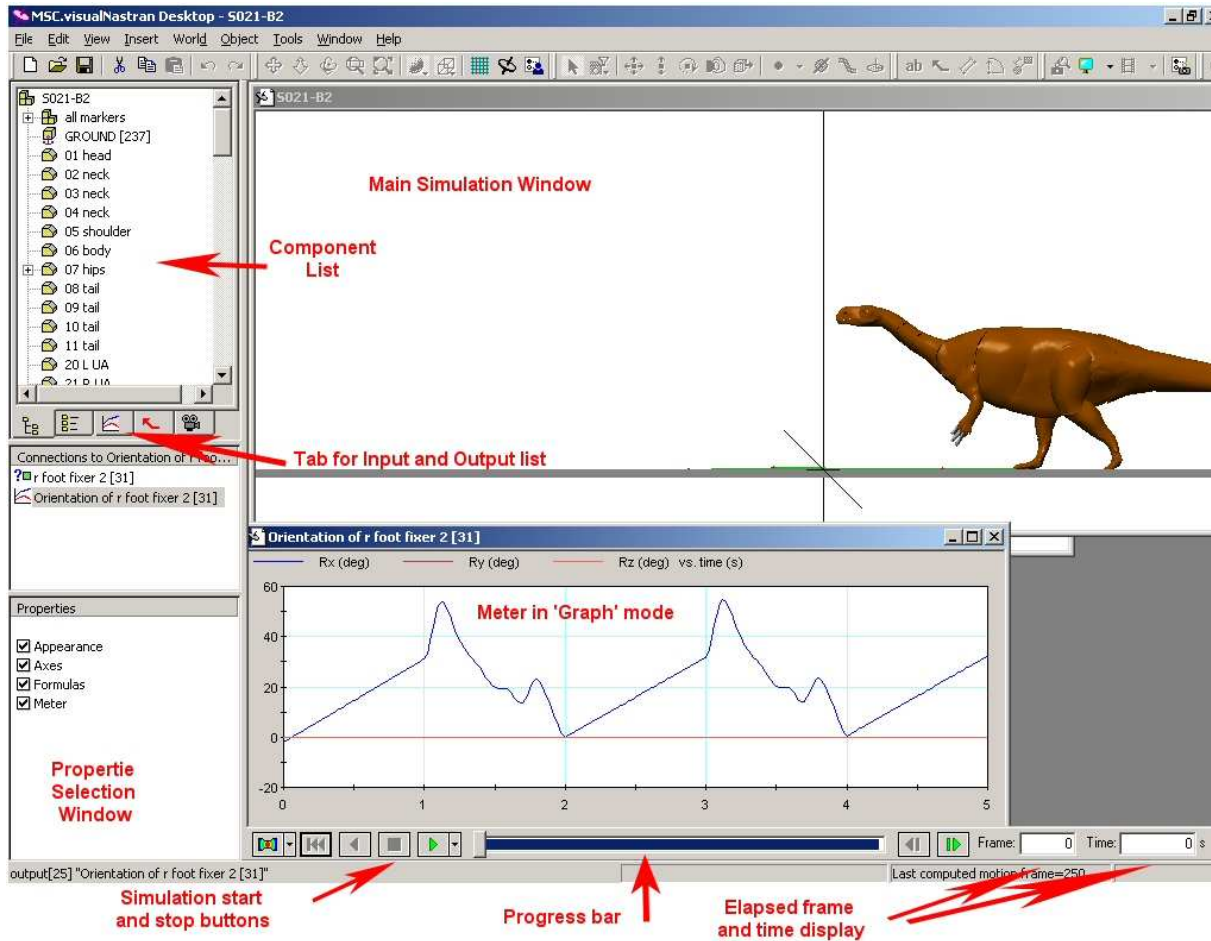


Figure 56: Screenshot of MSC.visualNastran 4D® work environment with a *Plateosaurus* simulation loaded. Important components are captioned.

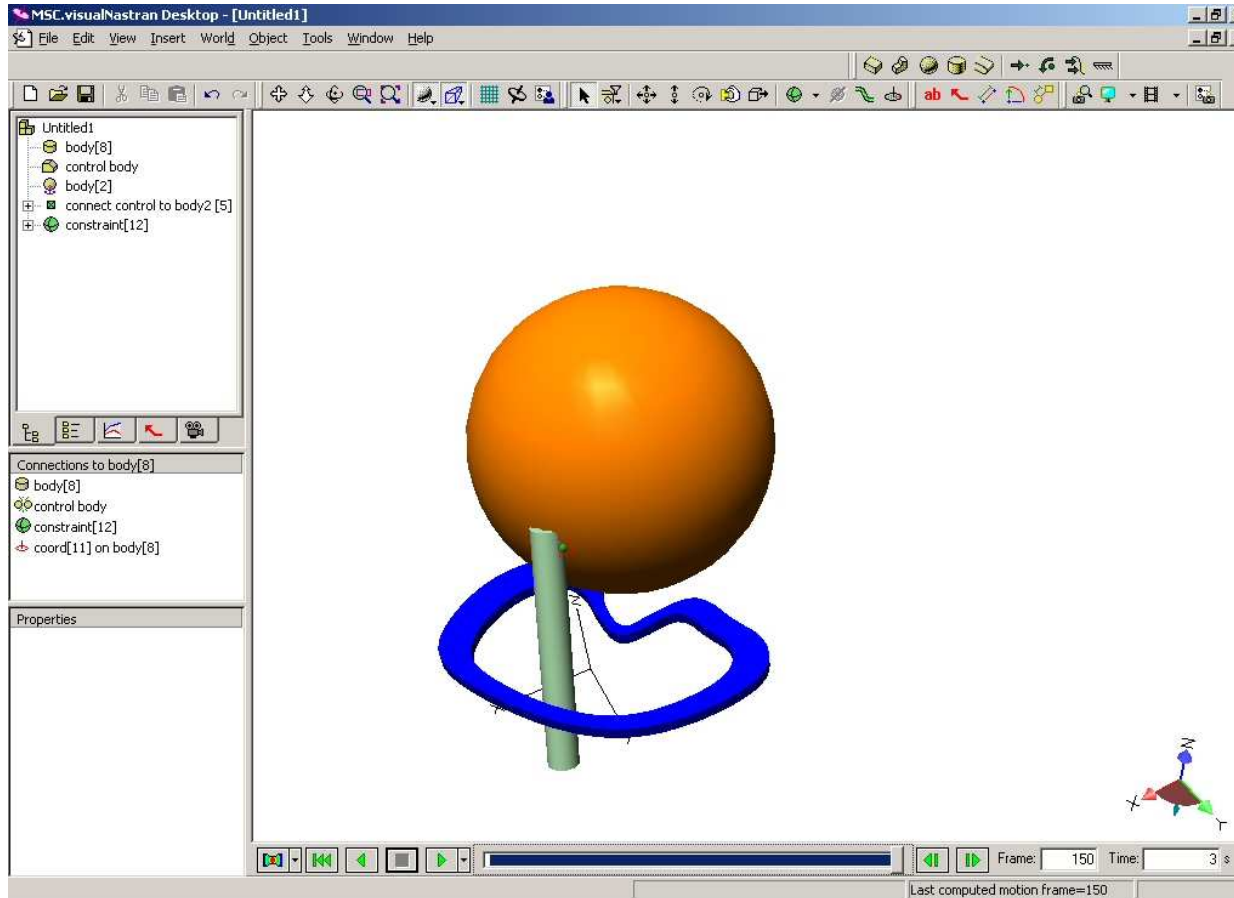


Figure 57: Example of a containing body to control the amount of rotation possible in a joint. The blue containing body limits the possible motion of the green cylinder, which otherwise rotates freely around all axes at the green [constraint].

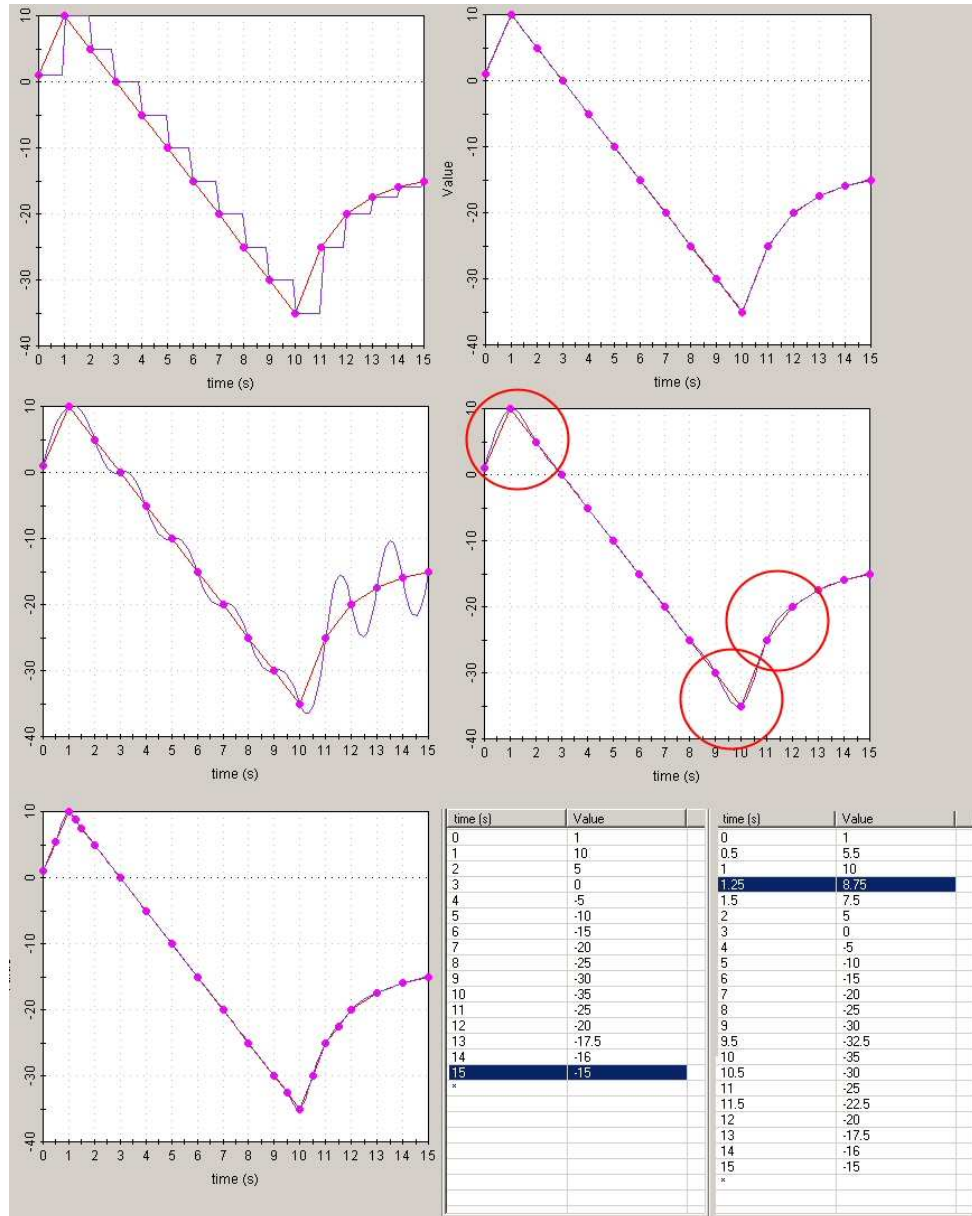


Figure 58: A table dataset (bottom right, left table) and the various options how MSC.visualNastran 4D® interpolates between the data points. Top left: piecewise constant, top right: piecewise linear, middle left: quadratic spline, middle right: cubic spline, bottom left: cubic spline with additional points. Bottom right shows the table with the added data points. Red circles mark places where the interpolated curve in the cubic spline differs from the linear curve significantly.

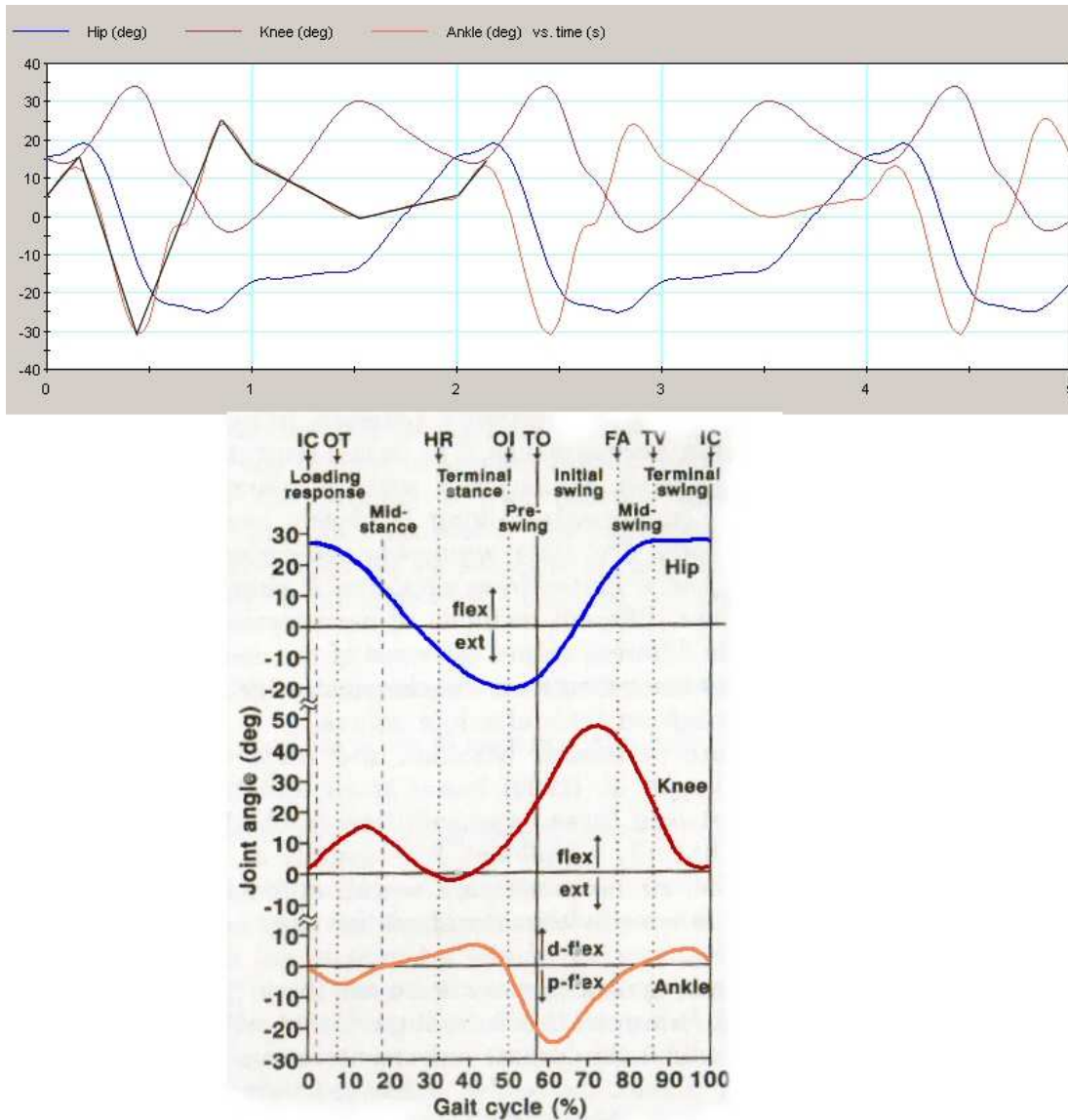


Figure 59: Top: Example of a meter graph of the orientation of the hip, knee and ankle of the optimized *Plateosaurus* walking cycle simulation model. The graph covers 2.5 iterations. In black, a stepwise linear curve has been superimposed over the actual curve of the ankle for the first cycle. Bottom: similar graph showing the sagittal plane joint angles during a single gait cycle of the hip, knee and ankle in a healthy human. Adapted from Whittle (1996). Note the rough similarity in the curve for the hips between both species, while the necessity to use mainly the knee to allow the foot to clear the ground forces the human to flex the knee much stronger than the dinosaur has to.

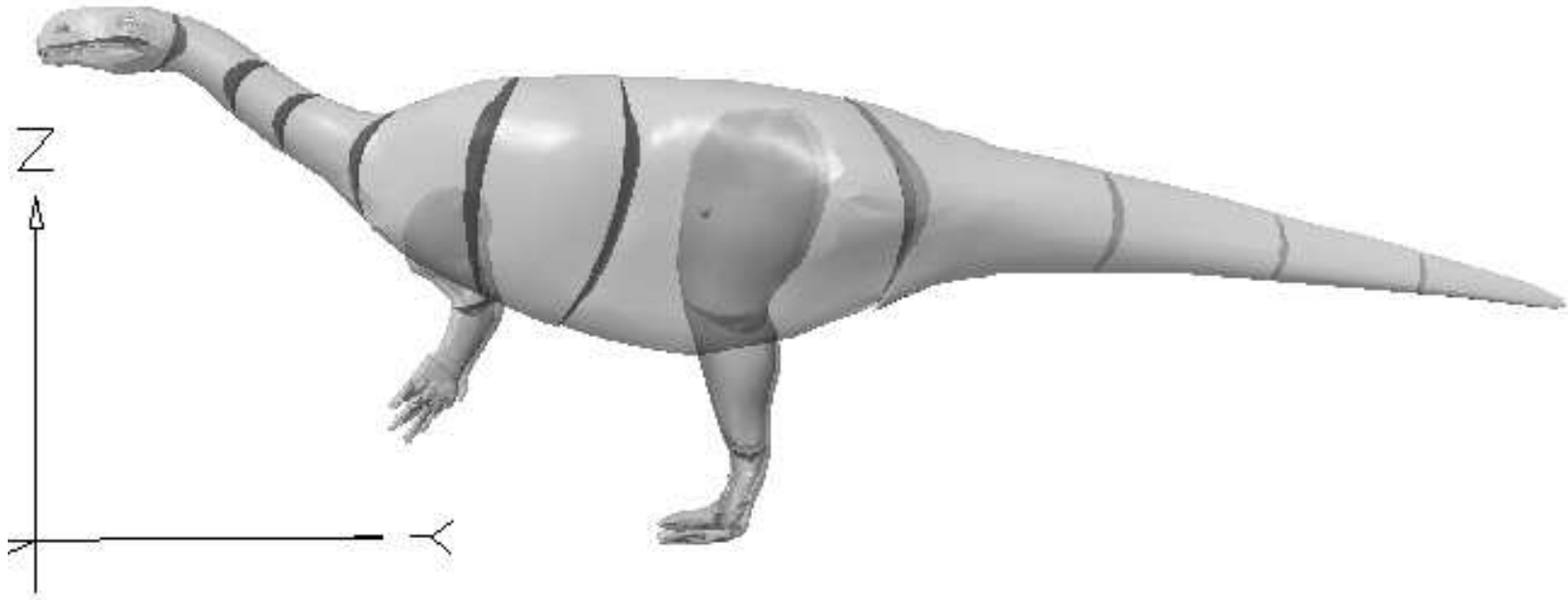


Figure 60: Center of mass of the *Plateosaurus* 3D model (small sphere) as calculated by MSC.visualNastran 4D® for uniform density

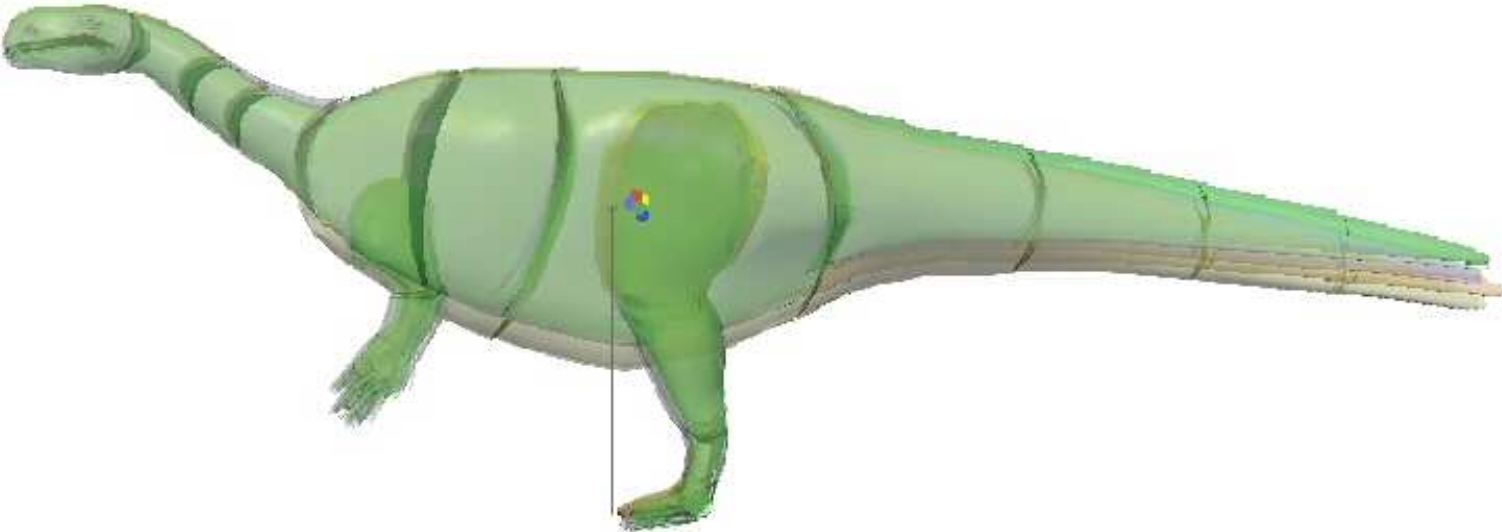


Figure 61: Superimposed views of the different *Plateosaurus* models. Colored dots indicate centers of mass. Note that only the center of mass of the model with a significantly thinner tail rests in front of the point of support.

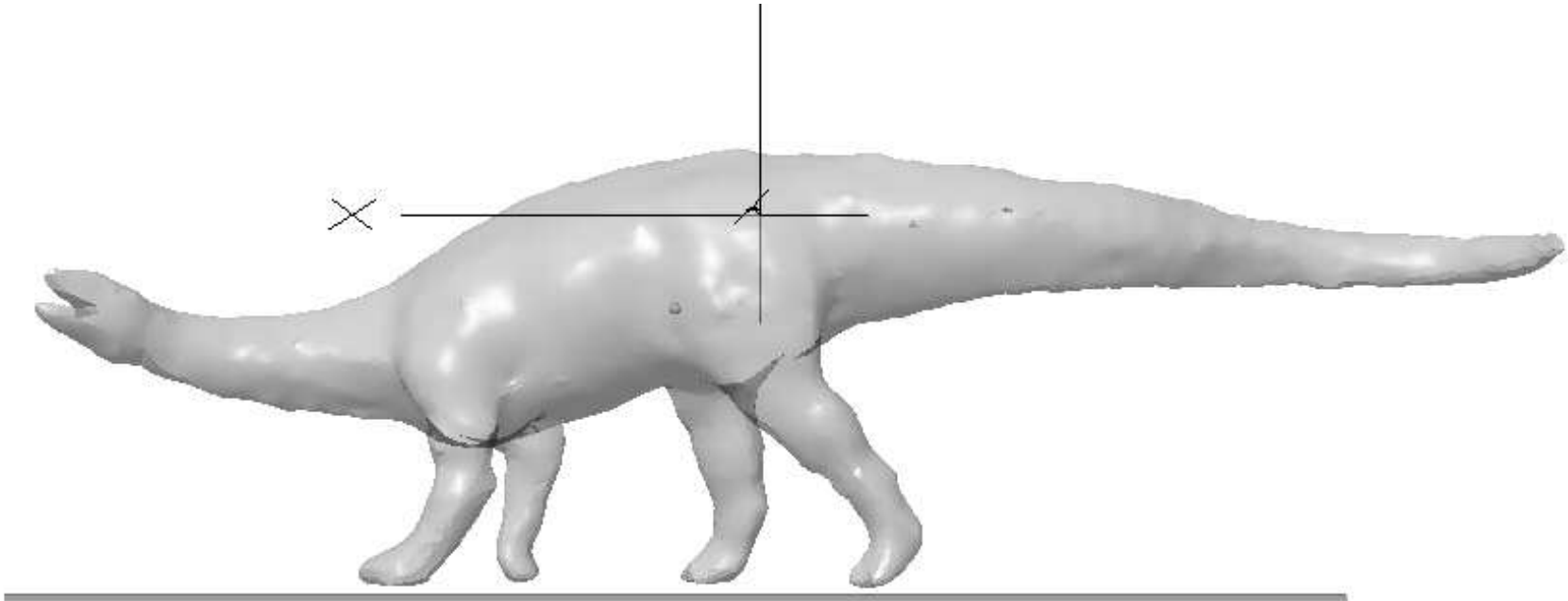


Figure 62: Toy model of Plateosaurus by Bullyland® with the center of mass calculated in MSC.visualNastran 4D®.

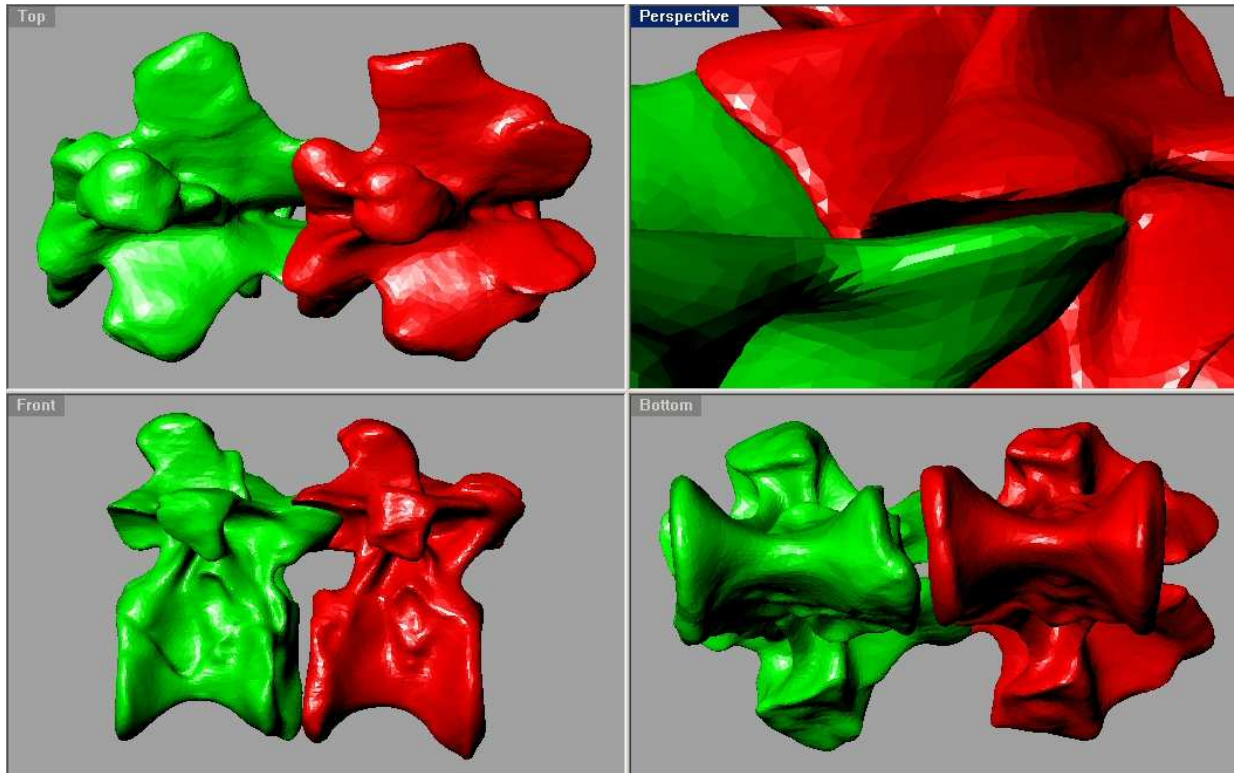


Figure 63: Dorsal vertebrae 2 and 3 of *Plateosaurus* in neutral articulation. Top left: dorsal view, bottom left: right lateral view, bottom right: ventral view. Top right shows a closer view of the zygapophysal articulation in oblique view.

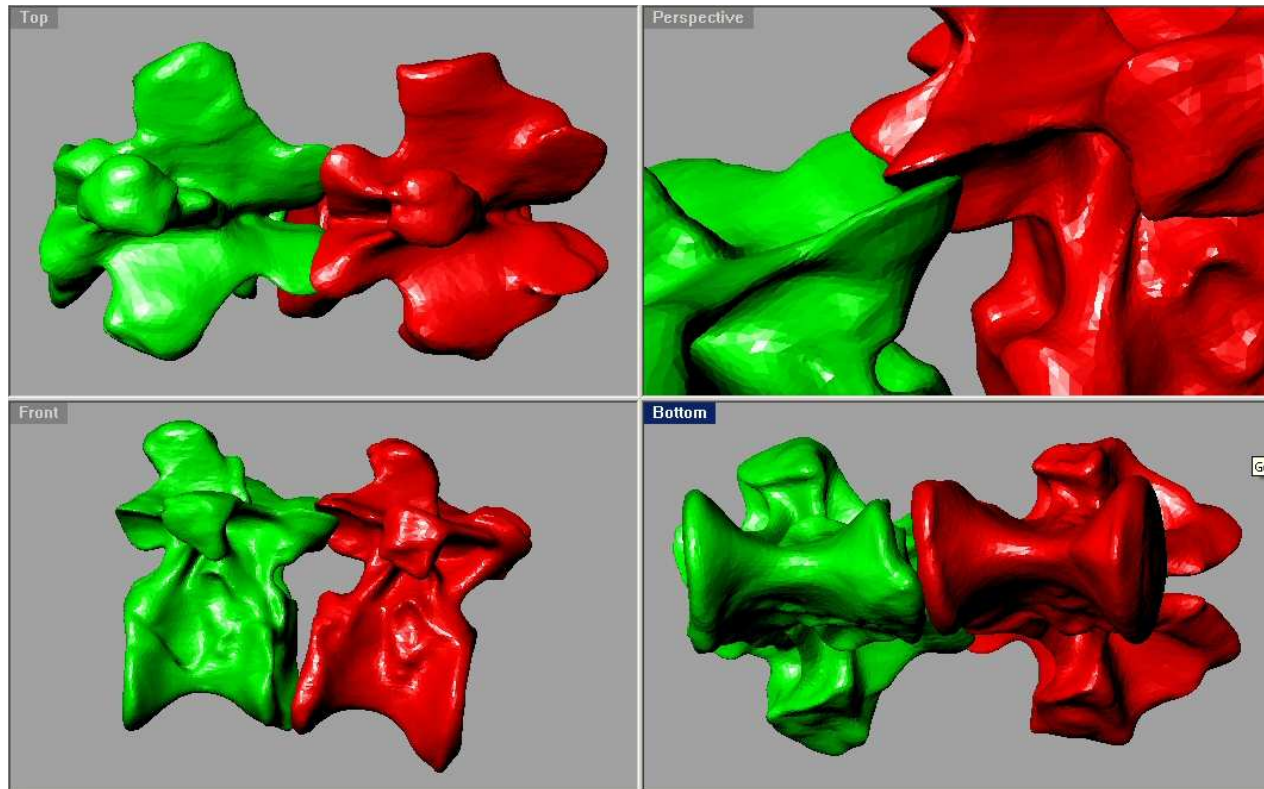


Figure 64: Dorsal vertebrae 2 and 3 of *Plateosaurus*. D3 has been rotated without disarticulating the bones. Top left: dorsal view, bottom left: right lateral view, bottom right: ventral view. Top right shows a closer view of the zygapophysal articulation in oblique view.

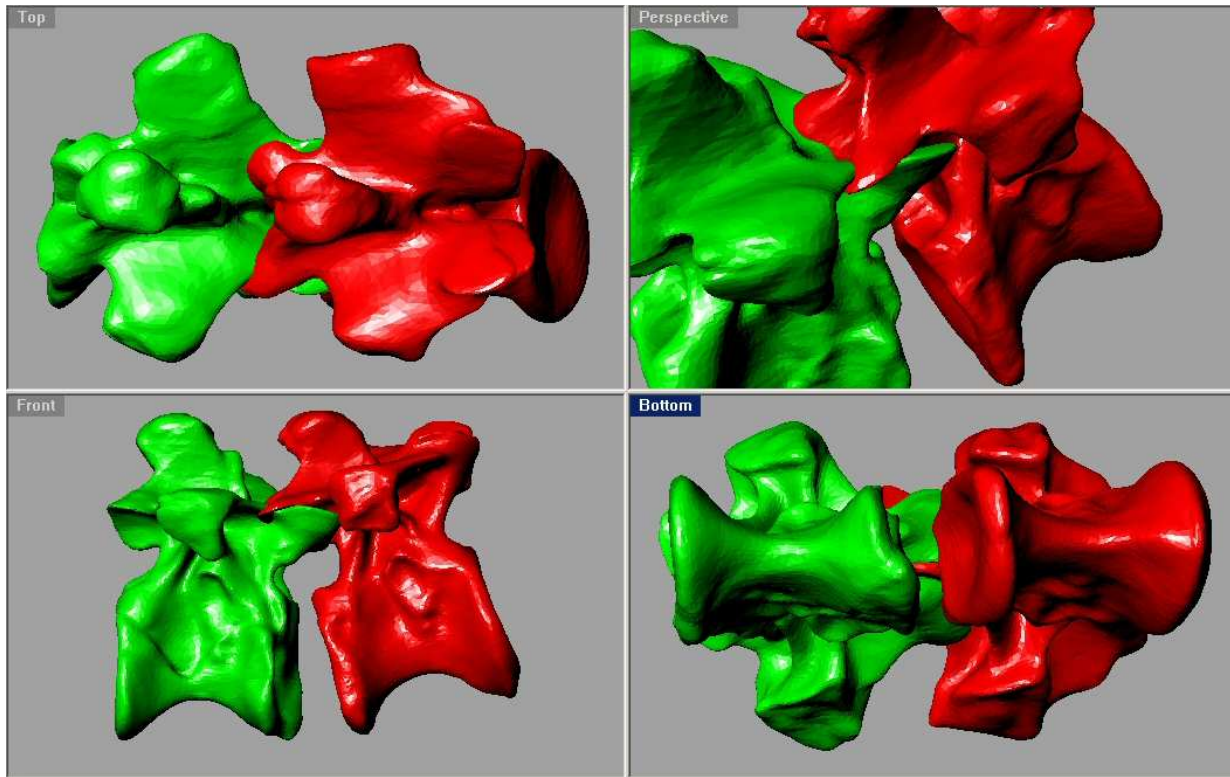


Figure 65: Dorsal vertebrae 2 and 3 of *Plateosaurus*. D3 has been rotated too much and intersects D2. Top left: dorsal view, bottom left: right lateral view, bottom right: ventral view. Top right shows a closer view of the zygapophysal articulation in oblique view.



Figure 66: A crocodile at the Stuttgart zoo shows the flexibility of its tail. Maximum values for lateral bending in Plateosaurus determined from virtual skeleton indicate a similar degree of bending was possible.

Mallison, H.: Virtual Dinosaurs - CAD and CAE Modeling Methods for Vertebrate Paleontology

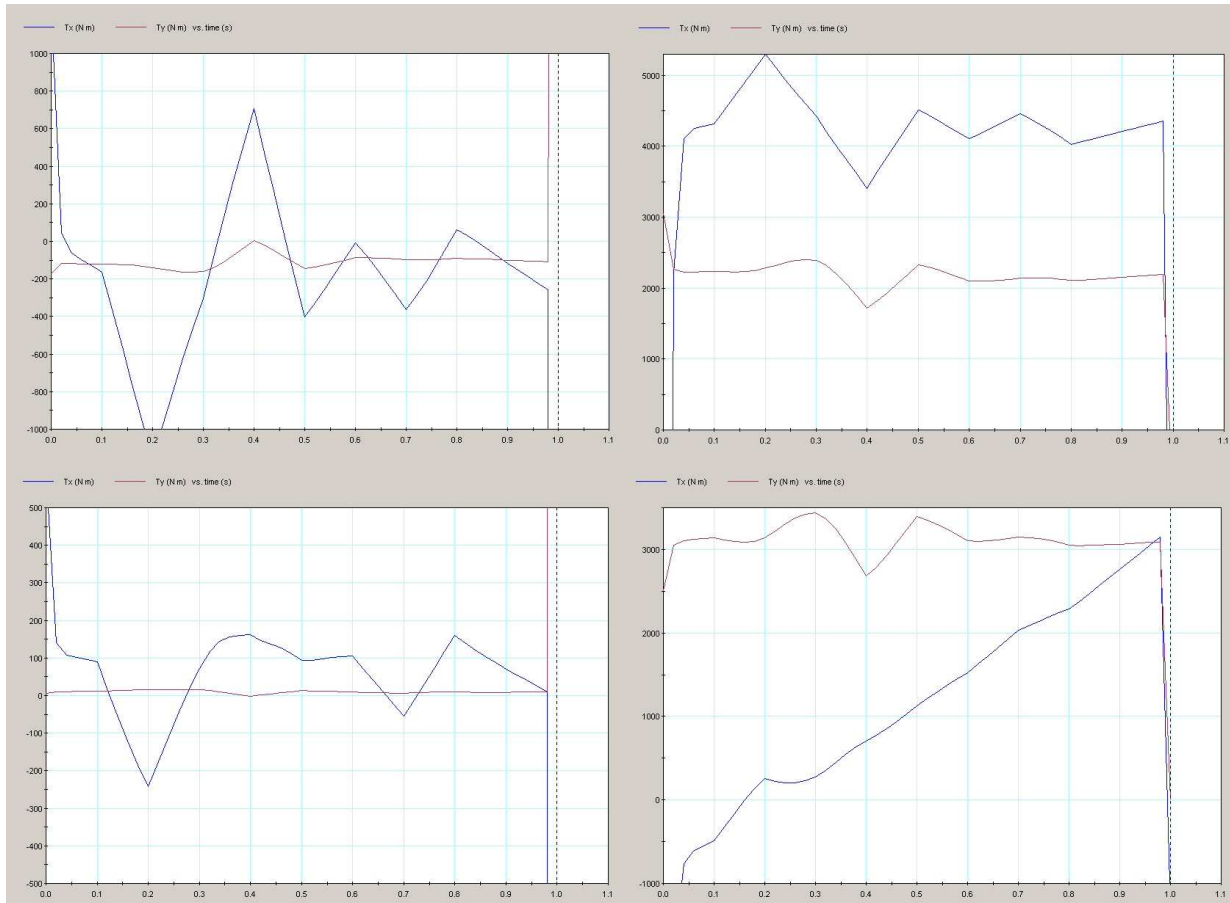


Figure 67: Meter graphs from simulation run S020. Top left: left hip, bottom left: left knee, top right: right hip, bottom right: right knee

Mallison, H.: Virtual Dinosaurs - CAD and CAE Modeling Methods for Vertebrate Paleontology

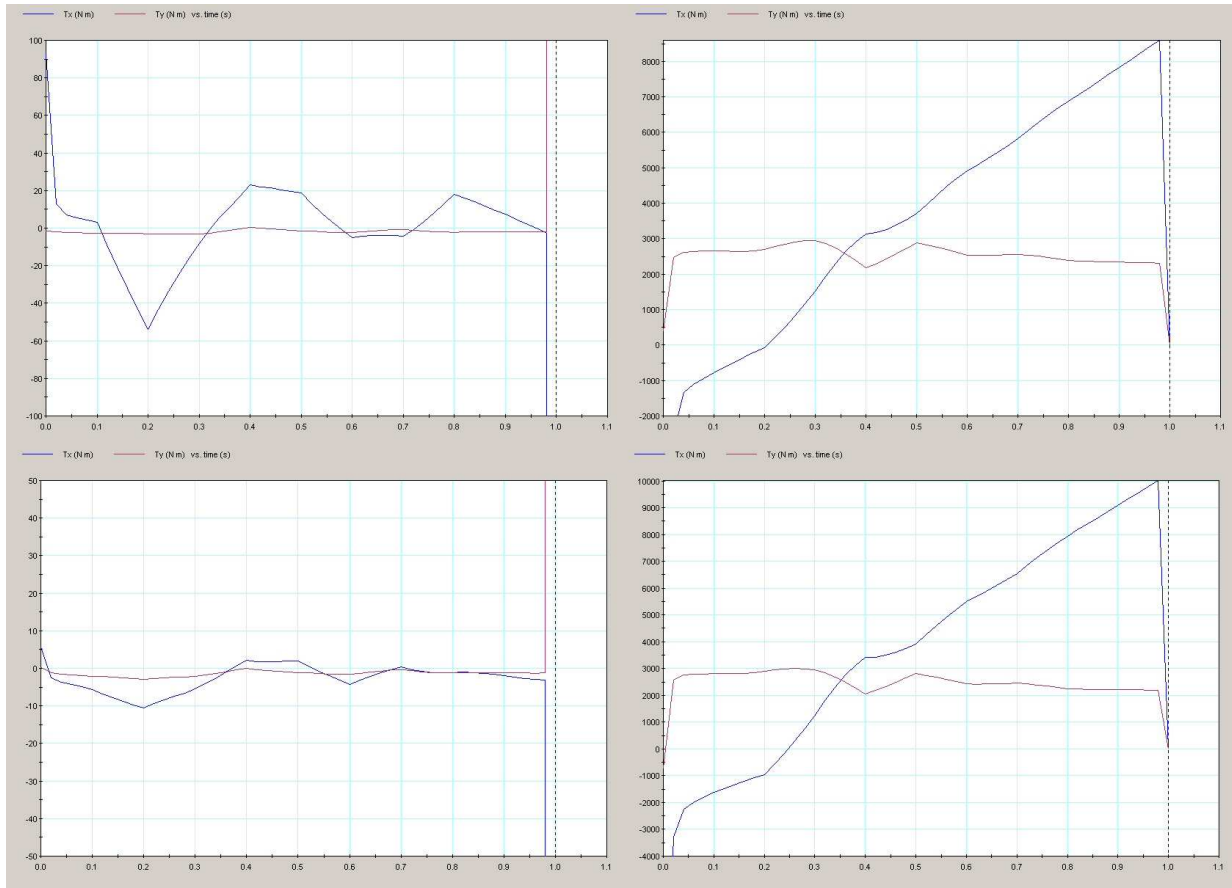


Figure 68: Meter graphs from simulation run S020. Top left: left ankle, bottom left: left toes, top right: right ankle, bottom right: right toes